Physics – Uspekhi **63** (10) 945 – 974 (2020)

REVIEWS OF TOPICAL PROBLEMS PACS numbers: **85.70.–w**, **85.75.–d**

Dielectric magnonics: from gigahertz to terahertz

S A Nikitov, A R Safin, D V Kalyabin, A V Sadovnikov,
E N Beginin, M V Logunov, M A Morozova, S A Odintsov,
S A Osokin, A Yu Sharaevskaya, Yu P Sharaevsky, A I Kirilyuk

DOI: https://doi.org/10.3367/UFNe.2019.07.038609

Contents

Abstract. **State-of-the-art studies of dielectric magnonics and magnon spintronics are reviewed. Theoretical and experimental approaches to exploring physical processes in and calculations of the parameters of magnonic micro- and nanostructures are described. We discuss the basic concepts of magnon spintronics, the underlying physical phenomena, and the prospects for applying magnon spintronics for data processing, transmission, and reception. Special attention is paid to the feasibility of boosting the operating frequencies of magnonic devices from the gigahertz to terahertz frequency range. We also discuss specific implementations of the component base of magnonics and ways to further develop it.**

Keywords: magnonics, spintronics, spin wave electronics, magnonic crystals, microwave electronics, magnetic structures, spin waves, waveguides, magnetic films, magnonic logic, data processing devices

S A Nikitov [1,2,3,a], **A R Safin** [1,4,b], **D V Kalyabin** [1,2,c], **A V Sadovnikov** [1,3,d], **E N Beginin** [3,e], **M V Logunov** [1,f], **M A Morozova** [3,g], **S A Odintsov** [3,h], **S A Osokin** [1,2,i], **A Yu Sharaevskaya** [1], **Yu P Sharaevsky** [3,j], **A I Kirilyuk** [1,5]
[1] Kotel'nikov Institute of Radio Engineering and Electronics, Russian Academy of Sciences, ul. Mokhovaya 11, kor. 7, 125009 Moscow, Russian Federation
[2] Moscow Institute of Physics and Technology (National Research University), Institutskii per. 9, 141701 Dolgoprudny, Moscow region, Russian Federation
[3] Chernyshevskii Saratov State University, ul. Astrakhanskaya 83, 410012 Saratov, Russian Federation
[4] National Research University Moscow Power Engineering Institute, ul. Krasnokazarmennaya 14, 111250 Moscow, Russian Federation
[5] FELIX Laboratory, Radboud University, Toernooiveld 7, Nijmegen, 6525, The Netherlands
E-mail: [a] nikitov@cplire.ru, [b] arsafin@gmail.com, [c] dmitry.kalyabin@phystech.edu, [d] sadovnikovav@gmail.com, [e] egbegin@gmail.com, [f] logunovmv@bk.ru, [g] mamorozovama@yandex.ru, [h] odinoff@gmail.com, [i] osokinserg@gmail.com, [j] sharaevskyyp@info.sgu.ru

Received 6 June 2019, revised 5 July 2019
Uspekhi Fizicheskikh Nauk **190** (10) 1009 – 1040 (2020)
Translated by M Zh Shmatikov

1. Introduction

More than three years have passed since our review [1] devoted to magnonics as a new research area in spintronics and spin-wave electronics was published in *Uspekhi Fizicheskikh Nauk* (*Physics–Uspekhi*). Over this time, the number of publications in this area has rapidly grown due to the first-rate scientific activity and the development of technologies that enable the creation of new materials and structures for studying new physical phenomena and the formation of a new, magnonics-based, component base. Several reviews have appeared in the same years, primarily in English-language journals, devoted to particular areas of magnonics and spintronics, including antiferromagnetic spintronics [2, 3], a new direction in spintronics — straintronics [4, 5], conceptual problems in creating a component base for a new type of memory for neuromorphic systems [6, 7], and magnonic crystals dedicated to processing information signals [8].

However, many other issues related to research in magnonics have been left aside. Moreover, the above reviews were primarily devoted to the results obtained by the authors of those publications. In this review, we consider a broad set of results following the style of our previous publication and

describe the problems that have emerged recently and are now actively discussed in the literature and at recent scientific conferences and workshops. This review is focused on the results obtained in magnonics or magnonic spintronics, which are primarily related to studies of dielectric materials. Such materials and, consequently, structures based on them do not contain electric charge carriers, implying that Joule losses are absent. Owing to this, the use of magnonic structures based on magnetic dielectric materials seems to be a very promising approach to creating an electronics component base using new physical principles.

The structure of the review is as follows. Section 2 presents fundamental results on dielectric magnonics. In particular, considered are the base designs of magnonic devices (Section 2.1), mathematical methods and numerical modeling employed to describe physical processes and to calculate the parameters of magnonic structures (Section 2.2), spin effects in magnonic micro- and nanostructures (spin transfer by magnons, spin Hall magnon effect, spin pumping, and thermal spin effects (Section 2.3)), topological magnonics (Section 2.4), and multilayer magnon heterostructures (Section 2.5). Sections 3–8 are devoted to research on magnonic crystals, experimental methods for studying magnonic structures, ferrite–semiconductor magnonic structures, domain walls and skyrmions in magnonics, magnonic oscillators and detectors, and terahertz magnonics. We discuss in the Conclusion (Section 9) the prospects for using magnonic structures to create a new component base and unsolved problems of magnonics that, in our opinion, are of interest.

2. Dielectric magnonics: a theoretical account

2.1 Basic designs of magnon devices for signal processing

Spin wave quanta (magnons) that propagate in magnetic materials can be used, owing to their unique properties, in promising systems for processing information signals with low energy consumption at various spatial and temporal scales. Low power consumption is ensured by the magnons being chargeless quasiparticles and Joule heat barely released in the process of their propagation in the magnetic dielectrics layers. Figure 1 shows a fairly general structure of a functional magnon element that converts an input signal $x(t)$ into an output signal $s(t)$ according to a given law F, i.e., $s(t) = F(x(t))$. The physical nature of the input and output signals is in this case of no importance: they may be electric, magnetic, optical, or other signals. It is of importance that the generation/detection of magnon fluxes propagating in the magnetic layer with frequency ω and wavenumber k occurs in localized spatial regions. Functional transformations F over the flux of magnons are performed in a spatially limited region by modulating the corresponding parameters of magnetic excitations: amplitudes, phases, frequencies, etc.

The natural scales for a functional element in the time domain are the periods of oscillations of magnetic excitations at ferromagnetic resonance: $T_r \sim 1/\omega_r$. The resonance frequencies ω_r, in the vicinity of which magnons at a given frequency ω of the input signal can be effectively generated, are known in [9] to be determined by internal static magnetic fields H: $\omega_r \sim H$. The internal magnetic fields, in turn, depend on both the material parameters of magnetic materials (saturation magnetization, type and magnitude of crystallographic anisotropy fields, etc.) and external magnetic fields. Using various types of magnetic materials (ferrites, spinels, antiferromagnets) in appropriate magnetic fields enables implementation of functional magnonic elements in a wide frequency range from dozens of MHz to hundreds of GHz with the transition to THz region.

The spatial scales in the functional element (see Fig. 1) are determined by the spin-wave wavelength $\lambda \sim 1/k$ at the frequency ω. Two classes of functional elements may be distinguished with respect to the ratio of the characteristic scale of the element L (for example, the distance between the input and output antennas) to the wavelength λ: localized, $L/\lambda \leqslant 1$, and distributed, $L/\lambda \gg 1$. The first class includes, for example, narrow-band filters, resonators, oscillators, and detectors, while the second has magnonic crystals, waveguides, interferometers, etc. For fixed internal fields, the wavenumber k and the frequency ω of the spin wave are coupled by the corresponding dispersion equations $D(k, \omega) = 0$. By changing the frequency ω, the wavenumbers can be varied over a wide range. The values of the wavenumbers can be distinguished in the spin-wave spectrum and conventionally separate the regions of dipole ($k < 10^5$ cm^{-1}), dipole-exchange ($10^5 < k < 10^6$ cm^{-1}), and exchange waves ($k > 10^6$ cm^{-1}) (see Fig. 1). Consequently, functional

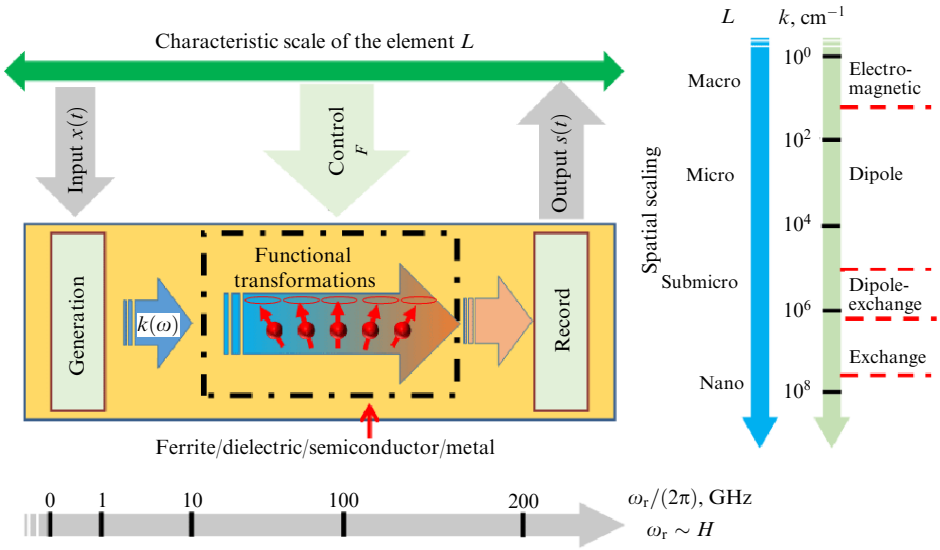

Figure 1. (Color online.) Generalized structure of a functional magnonic element.

elements with characteristic dimensions L can be effectively scaled in space, depending on the employed part of the spin wave spectrum, from the macrosize to nanosize range.

2.2 Mathematical methods for describing magnonic structures

Sections 2.2.1 and 2.2.2 briefly present several of the most popular methods used for mathematical modeling of magnonic structures. The development of new methods or adaptation of existing ones largely follows new technological options for creating experimental specimens. For example, since the first studies that describe periodic magnonic media — magnonic crystals (see Section 4) — appeared, many analytical methods have been developed based on techniques widely used to describe photonic crystals [10–12], which, in turn, were created in exploring periodic potentials of crystals in solid state physics.

An analytical method such as expansion in plane waves provides an accurate solution to the problem of magnon excitations in periodic structures that does not require resource-intensive calculations, but sets a number of restrictions on the geometry of the structures. A number of 'semi-analytical' and numerical methods enable the exploration of a wider class of irregular magnon structures; however, this approach requires the development of an original program code with a connection to libraries to solve systems of differential equations and handle linear algebra and the use of third-party open-source or proprietary software.

Numerical simulation methods turn out to be more demanding in terms of both computing capacities and subsequent processing of the collections of information obtained. Thus, the choice of the optimal method to analyze each particular magnonic structure depends on the infrastructure capacities available for numerical computation.

2.2.1 Analytical methods

I. *Group of methods of expansion in harmonics*

Plane wave method (PWM). This technique is a direct analogue of the weak coupling method in the electronic theory of solids [13–21] and one of the most popular methods applied to calculate the band structure of magnonic crystals due to the ease of its software implementation and good convergence. On the other hand, the PWM can only be applied to calculate strictly periodic structures. The convergence of the method also sharply deteriorates with an increase in the contrast of the material parameters of periodic media.

If a medium with periodically modulated material parameters is explored, the wave field can be represented in this method as a superposition of plane waves — Bloch harmonics with factors in the form of functions whose period coincides with that of the structure. Homogeneous waveguide eigenmodes are usually used as these functions. The material parameters are also expanded in a series, and the coefficients are found from the Fourier integrals over the cell. If the analytical form of the cell shape and inclusions is known, then arbitrarily complex geometries can be considered simply by increasing the number of harmonics in the expansion to compensate for the deterioration of convergence. The dispersion relation is derived from the fulfillment of the boundary conditions, which in this case looks like a solution to the eigenvalue problem.

We now consider the application of the PWM using as an example a one-dimensional bi-component magnonic crystal [20] magnetized tangentially in the Damon–Eshbach geometry [22] (Fig. 2). Since, in this structure, the saturation magnetization is a periodic function along the x axis, the magnetostatic potential can be expressed according to [23] in the form

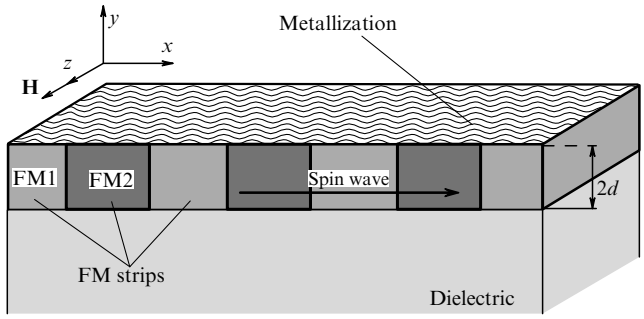

Figure 2. Spin waves in a one-dimensional magnonic crystal on a dielectric substrate with a metal contact on the upper surface. FM1 and FM2 are ferromagnetic strips with saturation magnetizations M_{s1} and M_{s2}, respectively.

$$\varphi(x,y) = \sum_p \Phi_p(y) \exp\left[\mathrm{i}(k+b_p)x\right] = \sum_p \Phi_p(y) \exp\left(\mathrm{i}k_p x\right), \tag{1}$$

where k is the Bloch wavenumber, $b_p = 2\pi p/a$ is the pth reciprocal lattice vector, a is the cell size, and $k_p = k + b_p = k + 2\pi p/a$. Components of the magnetic permeability tensor,

$$\hat{\mu} = \begin{bmatrix} \mu & \mathrm{i}\eta & 0 \\ -\mathrm{i}\eta & \mu & 0 \\ 0 & 0 & 1 \end{bmatrix}, \tag{2}$$

where

$$\mu = \frac{\omega_H(\omega_H + \omega_M) - \omega^2}{\omega_H^2 - \omega^2},$$

$$\eta = \frac{\omega_M \omega}{\omega_H^2 - \omega^2}$$

are also expanded into series:

$$\begin{aligned} \mu(x) &= \sum_p M_p \exp\left(\mathrm{i}b_p x\right), \\ \eta(x) &= \sum_p N_p \exp\left(\mathrm{i}b_p x\right). \end{aligned} \tag{3}$$

Coefficients M_p and N_p are found as follows:

$$\begin{aligned} M_p &= \frac{1}{a}\int_0^a \mu(x) \exp\left(-\mathrm{i}b_p x\right) \mathrm{d}x, \\ N_p &= \frac{1}{a}\int_0^a \eta(x) \exp\left(-\mathrm{i}b_p x\right) \mathrm{d}x. \end{aligned} \tag{4}$$

It is at this stage that the geometry of the specimen is taken into account. The way in which components with different magnetic susceptibility are located inside the unit cell is 'incorporated' into the amplitude coefficients of harmonics in integrating over the cell.

The test functions $\Phi_n(y)$ have not yet been determined, but it is logical to choose them to be similar to the spin wave functions in a homogeneous magnetic film. Then, substituting the test functions into Maxwell's equations in the

magnetostatic approximation [9] and renumbering and reducing similar terms, we obtain for each fixed m

$$\sum_n M_{m-n} k_n k_m \Phi_n(y) = \sum_n \left[\lambda^2 M_{m-n} \pm \lambda N_{m-n} b_{m-n}\right] \Phi_n(y) \,. \quad (5)$$

By introducing a new vector twice the length of the eigenvector $\mathbf{X}$,

$$\mathbf{Y} = \begin{bmatrix} \mathbf{X} \\ \lambda \mathbf{X} \end{bmatrix},$$

the nonlinear eigenvalue problem (5) can be reduced to a linear one:

$$\begin{bmatrix} \hat{M}_1 & 0 \\ 0 & \hat{M}_2 \end{bmatrix} \mathbf{Y} = \lambda \begin{bmatrix} \pm \hat{M}_3 & \hat{M}_2 \\ \hat{M}_2 & 0 \end{bmatrix} \mathbf{Y} \,. \quad (6)$$

Solving this eigenvalue problem for a magnonic crystal and for regions above and below it, the magnetostatic potential can be represented as

$$\varphi(x, y) = \begin{cases} \sum_s A_s \sum_n \hat{U}^0_{ns} \exp(\mathrm{i} k_n x) \exp(-\lambda_s^0 y) \,, & d < y \,, \\ \sum_s \Big[B_s \sum_n \hat{U}^{11}_{ns} \exp(\mathrm{i} k_n x) \exp(-\lambda_s^{11} y) \\ \quad + C_s \sum_n \hat{U}^{12}_{ns} \exp(\mathrm{i} k_n x) \exp(\lambda_s^{12} y) \Big] \,, & -d < y < d \,, \\ \sum_s D_s \sum_n \hat{U}^2_{ns} \exp(\mathrm{i} k_n x) \exp(\lambda_s^2 y) \,, & y < -d \,, \end{cases} \quad (7)$$

where A_s, B_s, C_s, and D_s are amplitude coefficients and $\hat{U}_{ns}$ is a matrix composed of eigenvectors. The number of Bloch harmonics taken into account in practical implementation, which is limited by the condition $-N \leqslant n \leqslant N$, determines the size of the matrix equations and must be increased in the case of large material or geometric contrasts in the unit cell of the structure.

The next step is to select the amplitude coefficients A_s, B_s, C_s, and D_s to satisfy the boundary conditions, namely, the continuity of the magnetostatic potential and the normal component of the magnetic induction vector. The boundary conditions may be presented as

$$\begin{aligned} &\left(\varphi^1(x, y)\right)\big|_{y=d} = \left(\varphi^0(x, y)\right)\big|_{y=d} \,, \\ &\left(\mathbf{B}^1_y(x, y)\right)\big|_{y=d} = \left(\mathbf{B}^0_y(x, y)\right)\big|_{y=d} \,, \\ &\left(\varphi^1(x, y)\right)\big|_{y=-d} = \left(\varphi^2(x, y)\right)\big|_{y=-d} \,, \\ &\left(\mathbf{B}^1_y(x, y)\right)\big|_{y=-d} = \left(\mathbf{B}^2_y(x, y)\right)\big|_{y=-d} \,, \end{aligned} \quad (8)$$

where $\mathbf{B}^1_y(x, y) = \{\hat{\mu} \nabla \varphi^1(x, y)\}_y$, $\mathbf{B}^{0,2}_y(x, y) = \{\nabla \varphi^{0,2}(x, y)\}_y$.

Substituting expansions (3) and (7) into boundary conditions (8), we obtain a set system of $8N + 4$ equations for the amplitude coefficients:

$$\hat{F} \begin{bmatrix} A_s \\ B_s \\ C_s \\ D_s \end{bmatrix} = \hat{0} \,. \quad (9)$$

A homogeneous set of linear equations is known to have a series of nontrivial solutions (the result of any linear transformation of solutions of the equation of motion is also a solution) if and only if the determinant describing this system is zero:

$$\det \hat{F} = 0 \,. \quad (10)$$

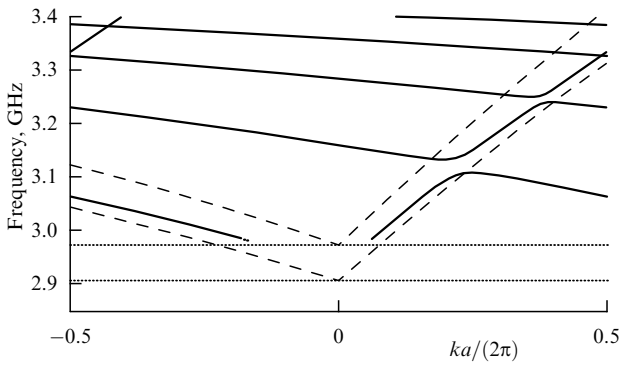

Figure 3. Dispersion curves of spin waves in a nonreciprocal magnonic crystal (see Fig. 2) (solid lines). Dashed lines correspond to the Damon–Eshbach modes for homogeneous ferromagnetic films with saturation magnetizations M_{s1} and M_{s2}; the dotted lines show the lower boundary frequencies $\omega_{\perp 1,2} = \sqrt{\omega_H(\omega_H + \omega_{M_{1,2}})}$, where $\omega_{\perp 1,2}$ is the limiting frequency for spin waves in a tangentially magnetized film that propagates perpendicular to the field direction.

By fixing a certain value of k and iterating the PWM algorithm for each value of ω from a certain set to satisfy Eqn (10), we obtain the dispersion curves of spin waves $\omega(k)$ in a nonreciprocal magnonic crystal (Fig. 3).

Coupled mode method. Another method to describe periodic magnonic structures is the technique [20, 24, 25] based on the coupled mode theory (CMT) [26]. Spin waves in a structure are described in this method as a superposition of two coupled waves propagating in opposite directions:

$$\begin{aligned} \varphi^1 = {} & A_+ \left\{ \exp\left[p_+(y - d)\right] + \alpha_+ \exp\left[-p_+(y + d)\right] \right\} \exp(\mathrm{i} q x) \\ & + A_- \left\{ \exp\left[p_-(y - d)\right] + \alpha_- \exp\left[-p_-(y + d)\right] \right\} \exp\left[\mathrm{i}(q - Q)x\right] , \end{aligned} \quad (11)$$

where $p_+ = q = Q/2 + \delta$, $p_- = -q + Q = Q/2 - \delta$, and the value of δ is chosen to be small.

Further, taking into account the boundary conditions, just as was done in the above method of expansion into plane waves, we obtain a 2×2 set of linear equations for the amplitude coefficients, from which the dispersion dependences of spin waves can be found.

The described method can only be applied for $q \approx Q/2$. Thus, it turns out that CMT is an analog of PWM that takes into account the first two Bloch harmonics, with a significantly restricted range of wavenumbers.

Tight binding approximation (TB). Less widely used is the tight binding approximation [27–31] developed by analogy with the approximation of strongly coupled electrons [32], according to which the Hamiltonian H of the system can be approximated by the Hamiltonian of an isolated atom concentrated at a crystal lattice site. In this approximation, it is possible to calculate the modes of magnonic crystals with localized and extended defects (in particular, for semi-infinite models of magnonic crystals or spatially bounded periodic structures). The field $\mathbf{H}$ near such a defect is expanded into localized wave functions that are obtained from the Wannier functions for a magnonic crystal without a defect:

$$\mathbf{a}_n(\mathbf{R}, \mathbf{r}) = \frac{\Omega^{1/2}}{(2\pi)^{3/2}} \int_{\mathrm{BZ}} \mathbf{H}_n(\mathbf{k}, \mathbf{r}) \exp(-\mathrm{i}\mathbf{k}\mathbf{R}) \, \mathrm{d}\mathbf{k} \,, \quad (12)$$

where the integral is taken over the Brillouin zone (BZ) wavenumbers. The Wannier functions form a complete

orthogonal basis defined for each zone and unit cell and only depend on the value $\mathbf{r} - \mathbf{R}$, where $\mathbf{r}$ is the space vector and $\mathbf{R}$ is the lattice vector. The inverse relation can be written as

$$\mathbf{H}_n(\mathbf{k}, \mathbf{r}) = \frac{\Omega^{1/2}}{(2\pi)^{3/2}} \sum_{\mathrm{G}} \mathbf{a}_n(\mathbf{R}, \mathbf{r}) \exp(-\mathrm{i}\mathbf{k}\mathbf{R}), \tag{13}$$

where the summation is carried out over the sites $\mathbf{R}$ of the crystal lattice G. The functions $\mathbf{H}_n(\mathbf{k}, \mathbf{r})$ are the eigenvectors of the equation of motion that describe the dynamics of $\mathbf{H}$. The PWM considered above can be used to obtain the functions $\mathbf{H}_n(\mathbf{k}, \mathbf{r})$ for a magnonic crystal without defects. To study a defect in a magnonic crystal, the field $\mathbf{H}(\mathbf{r})$ is represented as

$$\mathbf{H}(\mathbf{r}) = \sum_n \sum_{\mathbf{R}} c_n(\mathbf{R})\, \mathbf{a}_n(\mathbf{R}, \mathbf{r}). \tag{14}$$

A specimen of an antiferromagnetic topological insulator was studied in [28]. The energy spectrum of magnons was obtained in representing the magnon Hamiltonian using the TB method. Chiral edge modes localized near the specimen perimeter are also shown to exist for the energy range in which a bandgap was formed in bulk magnon modes, due to symmetry breaking, as a result of breaking the periodic lattice. It is with such parameters of the system for which these edge states coexist with the bandgap for bulk modes that they are topologically protected.

The TB method may be used to study the spectrum of magnons in yttrium iron garnet (YIG) at finite temperatures [30] taking into account the exchange interaction between the nearest neighbors. Spin degeneracy was described in [30] in analyzing thermal magnon excitation in the self-consistent field theory. The TB method can also be employed to take into account the effect of thermal magnon excitations on electronic conductivity in an antiferromagnet [31] due to an increase in the probability of electron–magnon scattering with increasing temperature.

II. *Group of multiple scattering theory methods*

The *multiple scattering theory* (MST) [1, 33–36] is a mathematical formalism used to describe the propagation of waves through an ensemble of scatterers. Examples of this process are the propagation of acoustic waves through a porous material, the scattering of light on water droplets in clouds, and the reflection of X-rays from a crystal. The main advantage of MST is the possibility of separating the individual properties of the scatterers and the periodicity of the inclusion lattice. This method does not set any restrictions on the contrast of material parameters of the medium and inclusions. However, a specific feature of the method is that it necessarily involves an explicit analytical calculation of the waves scattered by inclusions, which greatly restricts the area of its applicability; actually, inclusions may only be of a spherical and cylindrical shape, and the matrix should be an isotropic medium. The MST group includes a number of methods that enable a description of various types of magnonic structures. Some of these methods are presented below.

Transfer matrix method (TMM). One of the key differences between the MST formalism and PWM is the capability to consider spatially limited periodic structures. Thus, for example, some types of magnonic crystals with a finite number of periods have been considered using the TMM [37–39].

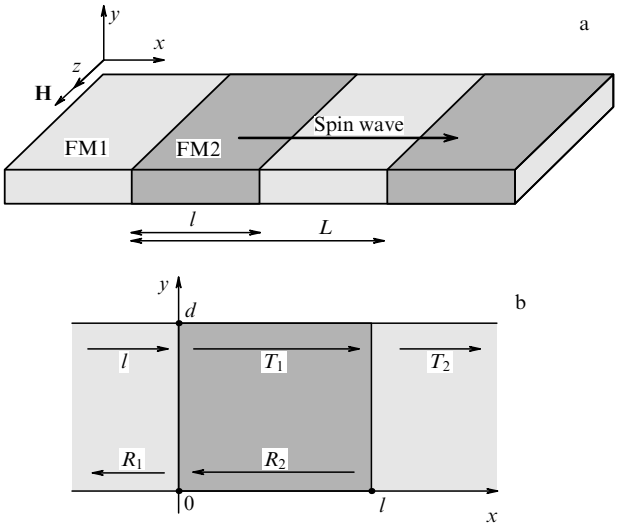

Figure 4. (a) One-dimensional magnonic crystal with a finite number of periods. (b) Signal transmission diagram.

We now consider the propagation of spin waves in a one-dimensional (1D) tangentially magnetized magnonic crystal which consists of ferromagnetic strips with various saturation magnetizations (Fig. 4a). The application of the TMM to a periodic structure involves finding a signal transfer function from one period of the structure to the next one (Fig. 4b), which can be expressed as

$$\begin{aligned} &\mathbf{Y}_{n+1} = \hat{T}\,\mathbf{Y}_n, \\ &\hat{T} = \hat{\Lambda}_n^{n+1}\,\hat{\Phi}_n, \end{aligned} \tag{15}$$

where $\hat{\Phi}_n$ is the matrix of the phase shift of the wave along one period,

$$\hat{\Phi}_n = \begin{pmatrix} \exp(\mathrm{i}k_n L) & 0 \\ 0 & \exp(-\mathrm{i}k_n L) \end{pmatrix}, \tag{16}$$

and $\hat{\Lambda}_n^{n+1}$ is an interface matrix that describes the scattering of the spin wave, which is obtained by satisfying the boundary conditions.

Applying the algorithm described above, it is possible to obtain in a recursive way the wave amplitude at the boundary of the Nth layer and, consequently, to calculate the dependence of the signal reflection coefficient on the wavenumber (Fig. 5). However, it should be taken into account, in this case, one period of the magnonic crystal (see Fig. 4), which consists of two ferromagnetic strips, should be considered a single layer.

Kronig–Penny model. A method similar to the Kronig–Penny model [40–44] can be considered a TMM modification; it describes a particle in a one-dimensional periodic potential, which, to simplify the problem, is assumed to be rectangular. Study [41] investigated, in particular, the propagation of spin waves in a 1D magnonic crystal that consists of ferromagnetic layers with various saturation magnetizations. It has been shown that a band structure is formed, and the transmission coefficients have been calculated in such magnon crystals and in the crystals containing defects. Notably, the motion of the electron in a 1D periodic potential in the presence of a spin-orbit coupling and a Zeeman field was considered in [44]. It is shown that, in addition to the conventional bandgaps at the

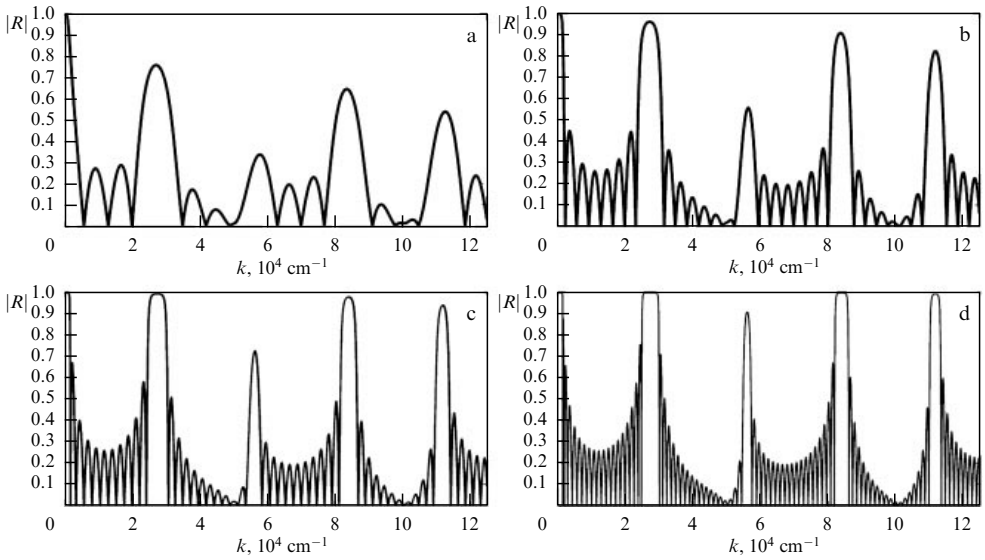

Figure 5. Band structure for magnonic crystals with various numbers of periods N: (a) $N = 4$, (b) $N = 8$, (c) $N = 12$, (d) $N = 20$. $M_1 = 1750$ G, $M_2 = 1850$ G.

Brillouin zone boundaries, additional bandgaps can form in this system inside the Brillouin zone.

2D MST/3D MST. The MST formalism can be applied not only in the 1D cases considered above, but also for various two-dimensional (2D) and three-dimensional (3D) magnonic crystals [45, 46]. In 2D and 3D cases, the phase advance during the propagation of scattered harmonics from one inclusion to another depends on the space vector $\mathbf{R}_i - \mathbf{R}_j$ rather than on the scalar, and the wave scattered on the inclusion can be expanded into the Bessel function basis. Review [1], in particular, presents in detail how the MST is applied to describe the propagation of spin waves in a ferromagnetic plate that contains an array of a finite number of ferromagnetic inclusions. Therefore, we do not dwell here on a detailed description of this method.

Effective environment approximations. Another method based on scattering theory is the coherent potential approximation (CPA) [47–51], which allows the concept of an effective medium to be introduced. This method may be used to replace a complex composite medium with an effective homogeneous medium, the parameters of which correspond to the effective material parameters of the composite. Thus, CPA makes it possible to calculate not only the dispersion of waves in a medium, but also the frequency dependence of the effective material parameters. In addition, dissipative material losses can also be taken into account. However, the geometry of the considered inclusions is again limited.

The use of the CPA is of greatest interest for describing such composite structures as metamaterials [52–55]. Metamaterials are usually understood as human-made environments that contain such frequency regions where the effective material parameter of the environment becomes negative. Metamaterials are usually formed by arrays of particles periodically located at the lattice sites. It is of importance that considered in such a structure is the propagation of waves whose lengths are much larger than the lattice period. The effective material parameters of the metamaterial significantly differ in this case from the material parameters of the constituent elements and depend on, among other things, the wavelength.

It was shown in [55] that a ferromagnetic film with an array of cylindrical cavities behaves like a magnonic metamaterial. It was proposed, in particular, to use such structures to create filters based on spin waves [45]: such filters do not feature strict correspondence between spin wave lengths and the period of the structure, while in filters based on magnonic crystals, where local resonance modes do not emerge, the spin wave lengths are rigidly tied to the period of the structure.

2.2.2 Numerical methods

Finite element method (FEM). An advantage of the numerical FEM [56] is its versatility, which makes it possible to calculate the dispersion of waves in structures with complex geometry and nonlinear and anisotropic elements that are not amenable to analytical consideration. Many software packages that implement FEM, including freeware, are now available. For example, FEM-based micromagnetic simulation can be carried out using the Comsol [21, 57–60], NMag [61], TetraMag [62], MagPar [63], and FastMag [64] software packages. In general, the FEM is applicable to a larger number of structure geometries than other numerical methods, but it is quite resource intensive.

We now consider a partial differential equation with a differential operator I of the order n, which acts on a function φ, and a source f:

$$I\varphi = f. \tag{17}$$

The first step is to approximate the function φ by a series of the form

$$\varphi = \sum_{j=1}^{N} c_j v_j\,, \tag{18}$$

where v_j are the given expansion functions and c_j are the constants to be determined. The solution of Eqn (17) is considered to be optimal, for which the residual $r = I\varphi - f$ is minimal at the points of the region Ω. According to the method of weighted residuals,

$$R_i = \int_\Omega \omega_i r\,\mathrm{d}\Omega = \sum_{j=1}^{N} c_j \int_\Omega \omega_i (I v_j - f)\,\mathrm{d}\Omega = 0\,. \tag{19}$$

The weight functions ω_i are functions of previous approximations. The problem can be represented in the matrix form:

$$\sum_{j=1}^{N} c_j L_{ij} = b_i\,, \quad L_{ij} = \int_{\Omega} v_i I v_j \,\mathrm{d}\Omega\,, \quad b_i = \int_{\Omega} v_i f \,\mathrm{d}\Omega\,. \quad (20)$$

Thus, a linear system of equations is to be solved for the unknown c_j, the matrix elements of which are mostly zero. The main idea of the FEM is to divide the computational domain into small elements and use simple linear or quadratic functions to approximate the sought-after solution at each element. Triangular meshes may be selected for planar geometries. In 3D problems, the structure is split into tetrahedra. Figure 6a shows an example of solving the static problem of the distribution of the demagnetization field in a magnonic structure that consists of a ferromagnetic film with a cylindrical inclusion. Netgen [65], an auxiliary program for generating partition meshes, was used to represent the magnonic structure as a set of tetrahedra (Fig. 6b). The size of the tetrahedra can be varied to improve calculation accuracy or performance. The figure also shows that an adaptive mesh may be used, the step of which becomes smaller near structure inhomogeneities, thereby significantly reducing the requirements for computing power while maintaining acceptable accuracy. We obtain as a result the distribution of the demagnetization field in the inhomogeneous magnonic structure for the static problem (Fig. 6c).

The FEM can also be used to calculate dynamic problems in various magnonic structures with consideration for boundary conditions, the anisotropy of materials, the effect of magnetic moment transfer, spin currents, and conduction currents. In particular, the FEM can be applied by introducing periodic boundary conditions to explore periodic magnonic structures, wherein it is sufficient to calculate the magnetization dynamics in one period of the structure. For example, studies [59, 60] investigated the propagation of spin waves in 3D magnonic crystals made of meander-shaped YIG, which are magnetized tangentially and normally. It is shown that such substantially bulk structures can be used in magnonics for signal processing.

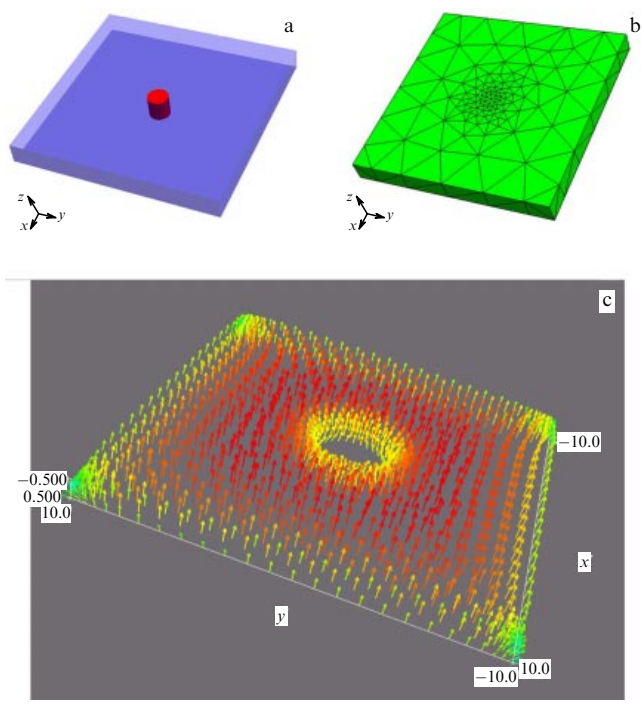

Figure 6. (Color online.) (a) Magnonic structure model and (b) mesh of its partition in the Netgen partition generator. (c) Distribution of the demagnetization field in a structure calculated using the NMag software package.

Finite-difference time domain method. Another popular numerical method to describe magnonic structures is the finite-difference time domain (FDTD) method [66, 67], in which differential equations are approximated by difference equations. The method is simpler to implement than the FEM, but it sets some restrictions on the geometry of the partition elements. We now consider its implementation in the general case of a conducting, isotropic, and homogeneous medium:

$$\frac{\partial \mathbf{E}}{\partial t} = \frac{1}{\varepsilon}\,\nabla \times \mathbf{H} - \frac{\sigma}{\varepsilon}\,\mathbf{E}\,, \qquad \frac{\partial \mathbf{H}}{\partial t} = -\frac{1}{\mu}\,\nabla \times \mathbf{E}\,. \quad (21)$$

Implementing the FDTD method, the first-order central finite difference is used in the finite-difference scheme for the derivative of the function:

$$\frac{\mathrm{d}u(x_i)}{\mathrm{d}x_i} = \frac{u(x_i + h) - u(x_i - h)}{2h} + o(h^2)\,. \quad (22)$$

Using this approximation in the 1D case and making replacements for curls and derivatives, and also taking into account that the medium under consideration is a magnetic dielectric (i.e., $\sigma = 0$), we arrive at a 1D scheme:

$$\frac{E_k^{n+1/2} - E_k^{n-1/2}}{\Delta t} = -\frac{1}{\varepsilon}\,\frac{H_{k+1/2}^{n} - H_{k-1/2}^{n}}{\Delta x}\,, \qquad \frac{E_{k+1/2}^{n+1} - E_{k+1/2}^{n}}{\Delta t} = -\frac{1}{\mu}\,\frac{H_{k+1}^{n+1/2} - H_{k}^{n+1/2}}{\Delta x}\,, \quad (23)$$

where Δx and Δt are the coordinate and time steps

$$E_k^n = E(n\Delta t, k\Delta x) = E(t, x)\,, \qquad H_k^n = H(n\Delta t, k\Delta x) = H(t, x)\,. \quad (24)$$

Thus, the **E** and **H** values are calculated in a stepwise manner. The obtained scheme can be generalized in an apparent way for two- and three-dimensional problems.

The FDTD method is realized using the OOMMF [68–70], MuMax3 [71], and GPMagnet [72] software packages. An interesting feature of the MuMax3 software package is that it implements the CUDA (Compute Unified Device Architecture) technology [73] that maintains distributed computing on Nvidia graphic processors, owing to which the program's performance is significantly boosted. The FDTD method implemented with MuMax3 was used in [59, 60, 74] both to calculate the distribution of static effective fields in 3D meander-shaped magnon crystals and to find the coefficients of transmission of spin waves through such crystals.

2.3 Spin effects in magnonic structures

We consider in this section the spin effects that manifest themselves in magnonic structures in the presence of a constant electric current, namely, the spin-moment transfer effect, the spin Hall effect, spin pumping, and thermal spin

effects (Seebeck and Peltier spin effects). These effects underlie the operation of electric current-controlled oscillators and detectors of microwave and terahertz oscillations (see Sections 7 and 8), spin wave waveguides based on domain walls, and neuromorphic processors (see Section 6). It should be noted that a fairly large number of review articles in English are available in the world's major journals that cover various aspects of spin effects associated with the motion of both conduction electrons (see, e.g., [75–77]) and 'pure' spin currents [78].

It has been shown rather recently that a spin current can be generated without the direct flow of an electric current through a magnetic material. Such a current can be created and carried by magnons in dielectric ferro- and antiferromagnetic materials. This phenomenon aroused some interest in the scientific community, since no Joule losses associated with conduction electrons occur in this case. Consequently, the term 'magnonics' was coined for this category of electronics and spintronics. It is on these phenomena that we focus our attention, which is the reason for the review title. However, to understand how spin is transferred by magnons, it is necessary to describe how this process occurs in 'conventional' spintronics, which is the subject of Sections 2.3.1 and 2.3.2.

2.3.1 Spin moment transfer. The flow of a high-density current of spin-polarized electrons, 10^6-10^{10} A cm^{-2}, through nanometer-thick ferromagnetic layers may result in a change in the direction of magnetization in such layers without the effect of an external magnetic field. This concept was first suggested theoretically in [79, 80] and experimentally confirmed in [81–84].

We now consider the concept of a model experiment (Fig. 7a) on the spin-transfer torque (STT) in a structure that consists of two ferromagnetic layers separated by a nonmagnetic conductor or insulator. A spin-polarized current of conduction electrons is formed in the F1 layer, and the magnetization of this layer is fixed at a certain angle with respect to the direction of magnetization in the F2 layer. When a spin current flows through F2, the exchange interaction between conduction electrons and ferromagnetic atoms aligns the spin polarization of the electrons along the direction of magnetization. The polarization component of the conduction electron spin, which is nonequilibrium for the F2 layer, is transferred to the atoms of the material through the s–d exchange interaction between the s-band electrons and localized d-electrons. The corresponding semiclassical energy density of the s–d exchange may be represented in the form [85–87]

$$W_{\rm sd} = -\frac{J_{\rm sd}}{M_{\rm s}}\,\mathbf{m}(\mathbf{r},t)\,\mathbf{M}(\mathbf{r},t)\,, \tag{25}$$

where $J_{\rm sd}$ is the exchange integral, $M_{\rm s} = |\mathbf{M}|$ is the saturation magnetization of the material, $\mathbf{m}$ is the magnetization of conduction electrons, and $\mathbf{M}$ is the magnetization of the lattice in F2. The dynamic of vector $\mathbf{M}$ in most magnetic materials may be considered slow compared to that of $\mathbf{m}$, and the s–d exchange results in the rotation of $\mathbf{m}$ around $\mathbf{M}$ and magnetic biasing of the conduction electrons along $\mathbf{M}$. The vector sum of the spins of the conduction electrons and lattice electrons should remain unchanged in the s–d exchange [85], while the nonequilibrium component $\delta\mathbf{m} = \mathbf{m} - \mathbf{m}_{\rm eq}$ is transferred to atoms of the F2 lattice, a phenomenon which may be

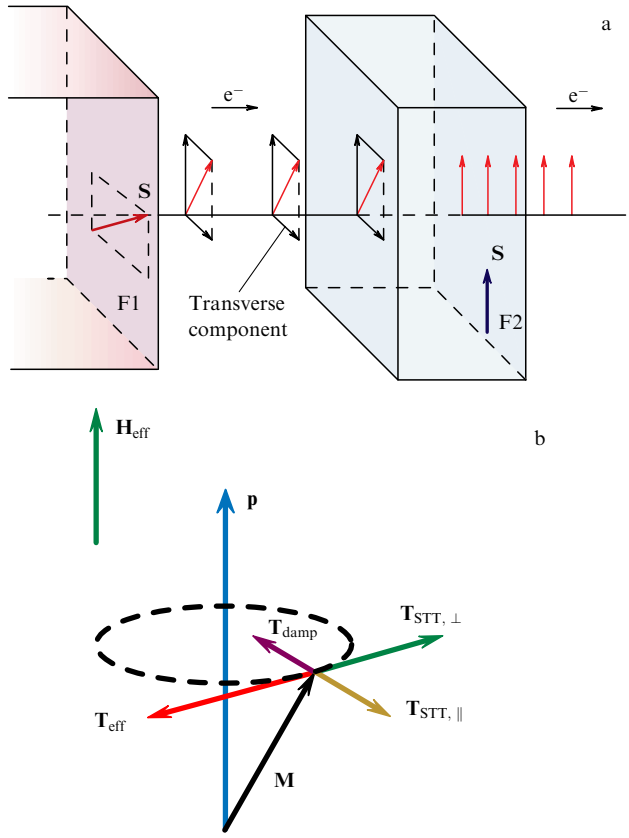

Figure 7. (a) Illustration of the concept of the transfer of spin moment **S** by an electric current from a layer with fixed magnetization F1 to a layer with free magnetization F2. (b) Dynamics of magnetization F2 in the presence of a spin current with polarization **p** fixed in the F1 layer.

represented as the effect of the spin-rotation torque $\mathbf{T}_{\rm STT}$ on $\mathbf{M}$.

Various approaches to the theoretical description of STT in ferromagnetic (FM) materials are currently available that vary from semiclassical models [85, 87, 88] to quantum mechanical techniques based on the spin-dependent scattering of conduction electrons on a potential created by localized torques [79, 89]. Most frequently used to describe the STT is the Landau–Lifshitz–Gilbert (LLG) equation, extended by introducing two components, $\mathbf{T}_{\rm STT,\parallel}$ and $\mathbf{T}_{\rm STT,\perp}$, that depend on current density:

$$\frac{{\rm d}\mathbf{M}}{{\rm d}t} = \gamma[\mathbf{H}_{\rm eff}\times\mathbf{M}] + \frac{\alpha_{\rm G}}{M_{\rm s}}\left[\mathbf{M}\times\frac{{\rm d}\mathbf{M}}{{\rm d}t}\right] + \mathbf{T}_{\rm STT}\,, \tag{26}$$

$$\begin{aligned}\mathbf{T}_{\rm STT} &= \mathbf{T}_{\rm STT,\parallel} + \mathbf{T}_{\rm STT,\perp}\\ &= \frac{g\mu_{\rm B}\varepsilon}{deM_{\rm s}^2}\,j_{\rm s}[\mathbf{M}\times[\mathbf{M}\times\mathbf{p}]] + \frac{g\mu_{\rm B}\varepsilon'}{deM_{\rm s}^2}\,j_{\rm s}[\mathbf{M}\times\mathbf{p}]\,.\end{aligned} \tag{27}$$

Here, γ is the absolute value of the gyromagnetic ratio, $\mu_{\rm B}$ is the Bohr magneton, g is the Landé factor for the electron, d is the thickness of the F2 free layer, e is the electron charge, $j_{\rm s}$ is the density of the spin-polarized current flowing into F2 from F1 with spin polarization $\mathbf{p}$, $\varepsilon = \varepsilon(J_{\rm sd})$, $\varepsilon' = \varepsilon'(J_{\rm sd})$ is the efficiency of spin polarization [79], $\alpha_{\rm G}$ is the Gilbert damping constant F2, and $\mathbf{H}_{\rm eff} = -\partial W/\partial\mathbf{M}$ is the effective magnetic field acting on $\mathbf{M}$ in F2 with a magnetic energy density W. The first term on the right-hand side of Eqn (26) describes the rotation of the magnetization $\mathbf{M}$ around the effective

magnetic field $\mathbf{H}_{\text{eff}}$, while the second term describes relaxation in F2. The terms $\mathbf{T}_{\text{STT},\parallel}$ and $\mathbf{T}_{\text{STT},\perp}$ in Eqn (27) characterize negative damping [79] and spin injection [85, 90] (the vector $\mathbf{T}_{\text{STT},\perp}$ is perpendicular to the $(\mathbf{M},\mathbf{p})$ plane), respectively (Fig. 7b). Usually [75], $\varepsilon' \ll \varepsilon$ and the second term in (27) can be ignored. Due to the STT, the magnetization $\mathbf{M}$ at high current densities can either flip, i.e., change direction to the opposite one, or switch to a state of stable precession of oscillations (oscillatory state). The oscillatory properties of such structures are discussed in Section 7. The estimated critical current at which the loss of stability occurs is [75]

$$j_{\text{th}} = \frac{deM_{\text{s}}}{g\mu_{\text{B}}\varepsilon}\,\alpha_{\text{G}}\omega_{\text{FMR}}\,, \tag{28}$$

where ω_{FMR} is the ferromagnetic resonance frequency in F2. The value of j_{th} for typical values of physical parameters is $10^8 - 10^9$ A cm^{-2}. Various attempts are being made at present to reduce the threshold current density by, for example, complicating the structure of the F1 and F2 layers [75, 85].

Magnetic dielectrics with low damping, for example, YIG, cannot be used in such structures, since conduction electrons do not propagate in dielectrics. However, a spin current can be generated without directly passing an electric current through the magnetic material. Next, we consider the structures in which the STT is generated due to the spin Hall effect in a nonmagnetic metal with strong spin-orbit coupling.

2.3.2 Spin Hall effect and spin pumping. M D'yakonov and V Perel' [91] were the first to show in 1971 that electric current carriers in semiconductors may be spatially separated according to their spin in the absence of a magnetic field. This phenomenon, referred to as the spin Hall effect (SHE) [92], was experimentally discovered in [93]. If an electric current $\mathbf{j}_{\text{e}}$ flows through a nonmagnetic metal (NMM) with strong spin-orbit coupling (for example, Pt, Ta, or W), a spin current $\mathbf{j}_{\text{s}}$ perpendicular to the $\mathbf{j}_{\text{e}}$ direction emerges due to multiple scattering of charge carriers [77]. This leads to the accumulation of electrons with a certain spin orientation on opposite surfaces of the conductor. The effect of the transfer of the spin current created in this way to neighboring layers is similar to the STT and is commonly called torque induced by spin-orbit coupling (spin-orbit torque, SOT), $\mathbf{T}_{\text{SOT}}$. A large number of experiments on the transfer of spin moment due to the SOT have been carried out in various nanostructures [94–98]. If the adjacent layer is a magnetic material (Fig. 8a) described by the magnetization vector $\mathbf{M}$, its dynamics are determined by the LLG equation of the form (26), in which the replacement $\mathbf{T}_{\text{STT}} \to \mathbf{T}_{\text{SOT}}$ should be made [76]:

$$\mathbf{T}_{\text{SOT}} = \mathbf{T}_{\text{SOT},\parallel} + \mathbf{T}_{\text{SOT},\perp}$$
$$= \frac{g\mu_{\text{B}}\eta\theta_{\text{SH}}}{deM_{\text{s}}^2}\,j_{\text{s}}\big[\mathbf{M}\times[\mathbf{M}\times\mathbf{p}]\big] + \frac{g\mu_{\text{B}}\eta'\theta_{\text{SH}}}{deM_{\text{s}}^2}\,j_{\text{s}}[\mathbf{M}\times\mathbf{p}]\,. \tag{29}$$

Here, θ_{SH} is a constant that characterizes the degree of the spin Hall effect in the conductor (spin Hall angle) and depends on the properties of the material: it is 0.1 for Pt, -0.07 for Ta, and -0.14 for W [99].

An important spintronic effect in ferromagnetic/nonmagnetic metal (FM/NMM) interfaces is spin pumping; namely, the rotation of the magnetization vector in the FM layer due to the spin-dependent scattering may result in the spin accumulation at the interface with the nonmagnetic metal and, thus, in a spin-polarized current from FM to NMM (Fig. 8b) directed perpendicular to the specimen plane (see details in [100–104]). Due to the presence of the spin current, an electric current emerges in the nonmagnetic metal, and a difference of potentials V_{SH} appears on opposite ends of the conductor, i.e., the inverse spin Hall effect occurs [76]. It should be noted that the output voltage contains both an invariable component U_{dc} that corresponds to a direct current and a variable component U_{ac} that corresponds to an alternating current. Thus, a mechanism is available that converts electric current into spin current and vice versa, owing to the direct and inverse spin Hall effect, respectively. The practical application of the spin Hall effect is primarily focused on controlling spin currents in solid-state micro- and nanostructures by means of electric currents and without using magnetic fields.

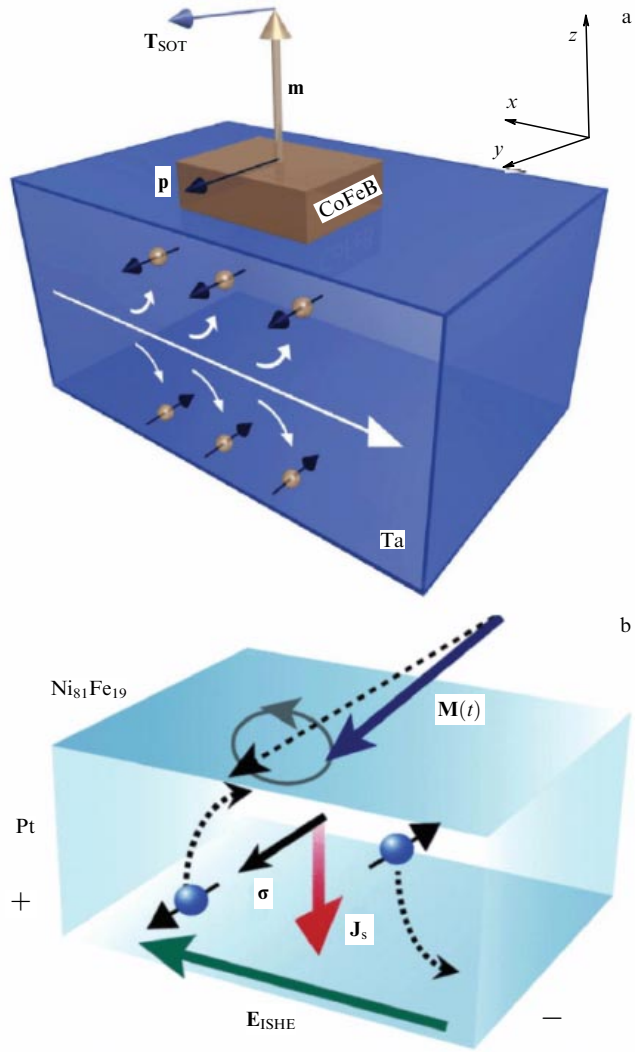

Figure 8. (Color online.) (a) Illustration of the transfer of spin momentum by means of spin-orbit interaction from a layer of nonmagnetic metal Ta to magnetic CoFeB [76]. (b) Spin pumping from a magnetic material $Ni_{81}Fe_{19}$ into a platinum layer [105]. Due to the inverse spin Hall effect, a potential difference arises at the opposite ends of the Pt layer, which is generated by the spatial separation of the spin-polarized electron current $\mathbf{J}_{\text{s}}$ ($\boldsymbol{\sigma}$ is the spin polarization vector) and the emergence of an electric field of intensity $\mathbf{E}_{\text{ISHE}}$.

2.3.3 Thermal spin effects. Studies of thermal spin effects that occur in magnonic nanostructures evolved into a new area of research which is commonly referred to as spin caloritronics.

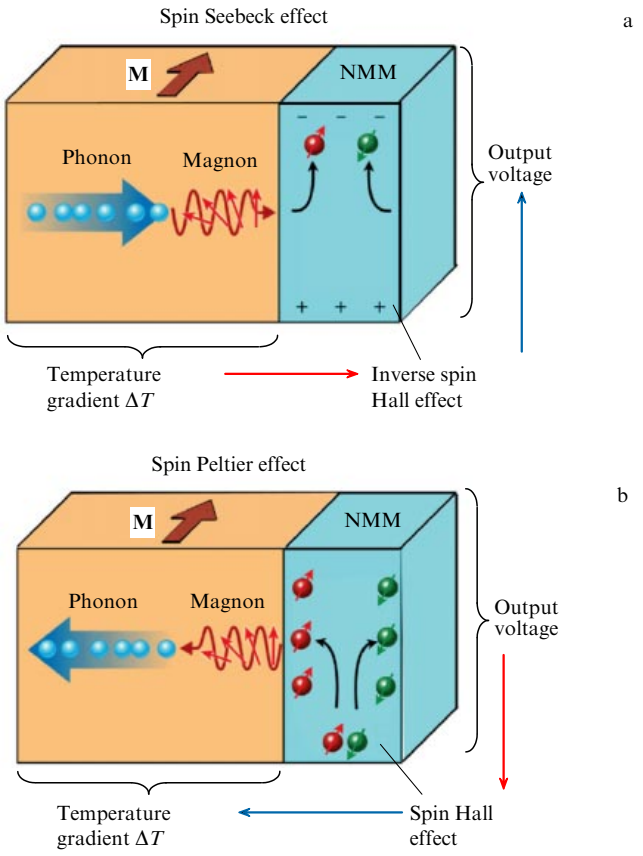

Figure 9. (Color online.) Illustration of the Seebeck (a) and Peltier (b) spin effects [76]. NMM is a nonmagnetic metal.

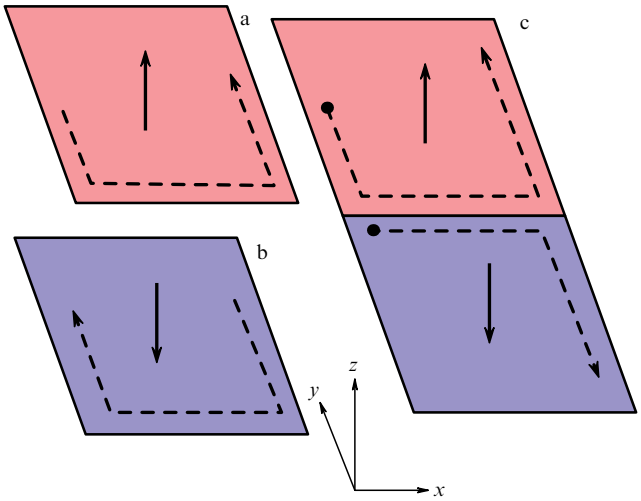

Figure 10. Ferromagnetic film with magnetization directed along (a) the $+z$ and (b) $-z$ axes. The dashed line denotes the allowed propagation path of edge waves at the film interface with a vacuum or another domain. (c) Schematic setup of a divider formed by two domains with opposite magnetization directions.

The spin Seebeck effect (SSE) [106], which occurs if the temperature gradient is oriented along the direction of magnetization of ferromagnetic material (Fig. 9a), consists of the separation of conduction electrons by spins. The temperature gradient causes the diffusion of electrons with different spin orientations with respect to the direction in which electrochemical potential decreases, which leads to the accumulation of electrons with opposite spins in different temperature regions of the ferromagnetic material. A spin current may be generated in this case in the nonmagnetic metal with and subsequently detected using the inverse spin Hall effect.

The spin-dependent Peltier effect [107] (Fig. 9b) may be considered a phenomenon inverse to the spin Seebeck effect. Electrons in the former effect that are in excess with respect to equilibrium electrons from a nonmagnetic metal diffuse into a ferromagnetic material due to a density gradient (here, magnetic dielectrics such as YIG may also be used). Heat outflow into the FM at the FM/NMM interface and a decrease in temperature in the NMM occur in this case. The density of spin-polarized electrons at the FM/NMM interface increases with an increase in the current density through the NMM; however, the increase in the relative temperature change due to the spin Peltier effect is limited by the release of Joule heat. In terms of quasiparticles, an interaction between magnons, caused by a spin current, and phonons occurs in the FM, generating a heat flux and a difference between temperatures. The efficiency of the spin Peltier effect is approximately an order of magnitude lower than that of the corresponding classical analogue [76]. Nevertheless, various options for using thermal spin effects for the generation of magnons [108] and the development of thermoelectric devices [109] have been proposed.

2.4 Topological magnonics

The development of technologies for the manufacture of thin magnetic films and nanoscale structures based on them has led to the emergence of studies of spintronic and magnonic devices based on topological effects [110–112]. Such devices operate using the properties of spin waves associated with the topology of magnetic structures, for example, with the emergence of dedicated directions for the propagation of spin waves and the exchange of energy between those waves in individual elements of devices. Dedicated structuring of magnetic films and material parameters and changes in boundary conditions enable structures to be created with preferred allowed or forbidden directions of propagation of spin waves [113] and control of their dispersion properties.

A manifestation of topological effects is the presence of chiral edge spin waves in ferromagnetic films with a hexagonal lattice. Such waves can propagate in a preferred direction in a waveguide channel formed by a film boundary [114] or domain walls [115] (see Section 6). Edge spin waves propagate in films with different directions of saturation magnetization (Fig. 10a, b) in mutually opposite directions along the domain boundary. If there is a boundary between domains (Fig. 10c), a spin wave has one general direction of propagation for both domains, and the spin wave of one domain excites magnetic oscillations in the other.

A design of a splitter [116, 117] and a spin wave (SW) interferometer on the basis of the nonreciprocity effect has been proposed. Two splitters are combined on the basis of a similar principle, one of which acts in the inverse direction, adding two spin waves with different phases due to the interference effect. There are two ways for a spin wave to propagate at the boundary of these domains in such an interferometer formed by two domains (Fig. 11). The phase shift between two spin waves is determined by the dispersion characteristics of the material along the paths of the SW passage and the position of the domain boundaries.

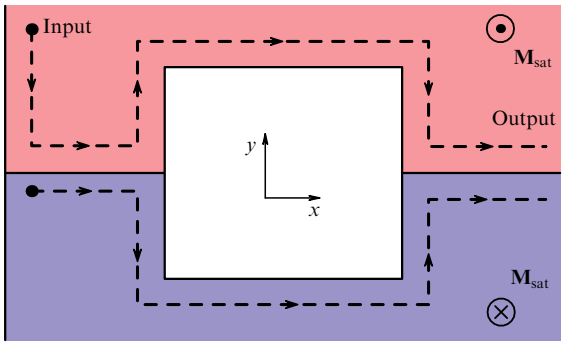

Figure 11. Schematic setup of an interferometer formed by two domains. The arrows indicate the propagation paths of edge spin waves along the domain boundaries.

Study [118] describes an option to create waveguide structures for topologically protected magnon modes using artificially structured films. A ferromagnetic YIG film with a periodic hexagonal lattice of triangular holes is proposed as a medium in which spin waves propagate. The slope of the hole relative to the unit cell determines the dispersion characteristics of spin waves, which depend on the direction of the wave vector. The role of walls between domains is played here by the boundary between regions with different angles of inclination of the triangular holes — a structure of this type, like domains with different directions of magnetization, has a dedicated channel for the propagation of spin waves, in which they can divide and interfere.

Another way to reconfigure magnonic devices is to create composite or discrete structures that consist of several spatially separated elements [119–123]. A divider of two waveguides, in which spin waves can exchange energy by means of dipole–dipole interaction, is described in [124] (Fig. 12). A spin wave excited in waveguide 1 excites a wave with an opposite phase in waveguide 2. Here, the structure of the topology can be varied by changing the direction of magnetization of an individual waveguide or by creating domain walls inside the waveguides. In a setup with two uniformly magnetized waveguides (in the same or opposite directions), the spin wave energy is swapped along the entire length of the exchange channel; thus, two coupled modes propagate. The fraction of SW energy in each waveguide depends at the output on the ratio of the amplitudes of coupled waves at the exit from the section with dipole–dipole interaction between these SWs. Thus, the output power of the magnetic oscillations of each waveguide is controlled by changing the frequency of the excited spin wave. A diode for spin waves is also proposed in [125] based on the nonreciprocity effect of SW propagation in a waveguide formed by a domain wall (see Section 6); other nonreciprocity effects in magnetic materials are also explored [126–128].

Study [129] theoretically investigated the frequency properties of waveguides formed by discrete ferromagnetic pillars (Fig. 13). Characteristics, such as the frequency dependence of the power in the output channels, can be controlled in such magnonic devices by changing the properties of individual elements. An array of cylindrical FM pillars located in a periodic way on a straight line [130] is considered as a waveguide. A model of the interaction of magnetic dipoles is applied to a system of N FM pillars, wherein each pillar is represented by a magnetic dipole with a magnetic

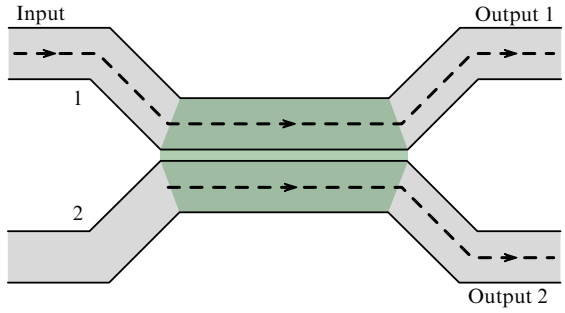

Figure 12. (Color online.) Two waveguides, 1 and 2, with an area (green color) in which energy is exchanged between coupled spin waves. A wave from one waveguide (input), when passing through the structure, is divided into two waves (output 1, output 2), the amplitudes of which depend on the wave frequency and dispersion characteristics of the medium.

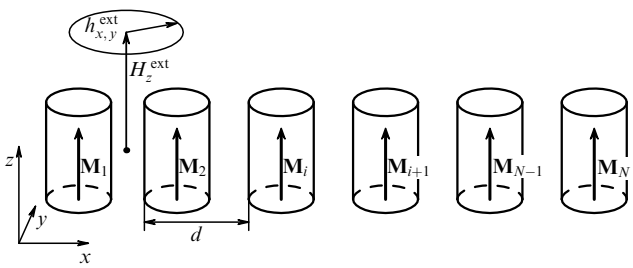

Figure 13. Chain of N FM pillars. H_z^{ext} is a constant external magnetic field, h_{xy}^{ext} is an alternating external magnetic field, and $\mathbf{M}_i$ is the magnetization vector of each of the pillars.

moment $\mathbf{M}_i = \mathbf{m}_i + \boldsymbol{\mu}_i$ ($\boldsymbol{\mu}_i = (0, 0, \mu_i)$, $\mathbf{m}_i = (m_i^x, m_i^y, 0)$). If the oscillation amplitude is small, $|m_i^x|, |m_i^y| \ll |\mu_i|$, a system of linearized Landau–Lifshitz equations for the saturation magnetization and an external alternating field with a small amplitude, $h^{ext}(t) \ll H^{ext}$, may be derived:

$$\mathrm{i}\omega\mathbf{m}_i + \gamma\mathbf{m}_i \times \mathbf{H}^{ext} - \mathrm{i}\alpha\hat{\mathbf{z}} \times \mathbf{m}_i + \gamma\mathbf{F}_{dd} = -\gamma\boldsymbol{\mu}_i \times \mathbf{h}^{ext}, \quad (30)$$

where $\mathbf{F}_{dd}$ is the linearized part of the strength of dipole–dipole interaction between the pillars that acts on the ith magnetic moment $\mathbf{M}_i$,

$$\mathbf{F}_{dd} = \sum_{j=1,\, i\neq j}^{N} \frac{V^*}{r_{ij}^3} \left[\boldsymbol{\mu}_i \times \frac{3(\mathbf{m}_j\, \mathbf{r}_{ij})\, \mathbf{r}_{ij}}{r_{ij}^2} - \boldsymbol{\mu}_i \times \mathbf{m}_j - \mathbf{m}_i \times \boldsymbol{\mu}_j + \mathbf{m}_i \times \frac{3(\boldsymbol{\mu}_j\, \mathbf{r}_{ij})\, \mathbf{r}_{ij}}{r_{ij}^2} \right]. \quad (31)$$

The frequency characteristics of the spin wave eigenmodes in such a structure depend on the configuration of the magnetization of individual pillars. The distance between the pillars and their arrangement on the plane (periodic arrangement along a straight line, in a circle, or in a random way) determine the nature of the dipole–dipole and exchange interactions. Thus, in the presence of anisotropy in the FM material or under the effect of exchange fields, adjacent pillars can retain opposite directions of magnetization. Due to these properties of the structures made of FM material, various configurations of magnetization may exist, which is one of the ways to control the properties of propagating spin waves. A uniformly magnetized chain of finite-length pillars has

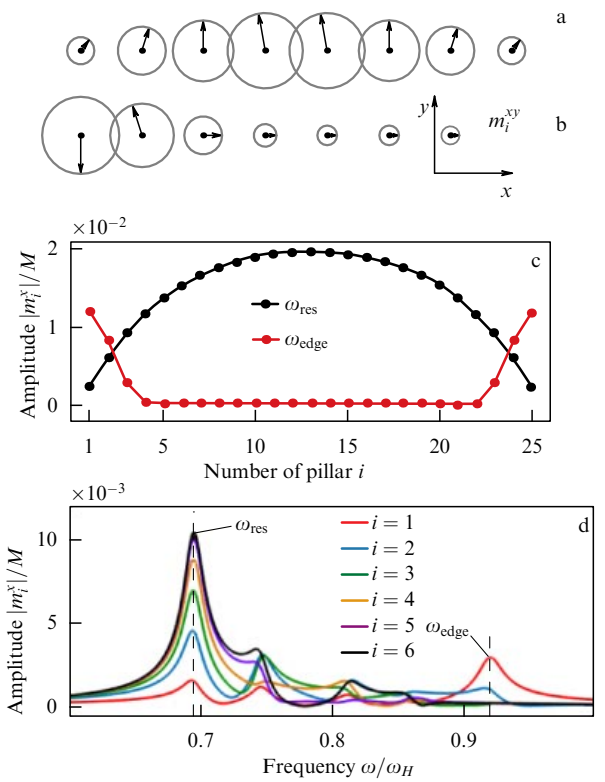

Figure 14. (Color online.) Distribution of the amplitude and relative phase of oscillations of magnetization m_i^{xy} in a chain for bulk (a) and edge (b) spin wave eigenmodes. (c) Comparison of both modes for a chain consisting of $N = 25$ pillars. (d) Amplitude m_i^x as a function of frequency ω for a pillar with number i; ω_{res} and ω_{edge} are resonance frequencies.

eigenmodes (Fig. 14), whose resonance frequencies for the FM configuration differ in the general case from those of an infinite chain.

The eigenfrequency values with the number $s = 1, 2, \ldots, N$ and the wavenumber $k = s\pi/[d(N+1)]$ under the boundary condition with free ends are found as follows [129]:

$$\omega_s^2 = \left[\omega_H + 2\Delta\omega\left(\cos\frac{\pi s}{N+1} - 1\right)\right] \times \left[\omega_H - 2\Delta\omega\left(2\cos\frac{\pi s}{N+1} + 1\right)\right], \quad (32)$$

where ω_H is the resonance frequency of an isolated pillar. The numerical solution of system of equations (30) yields the values of the effective interaction parameter $\Delta\omega$ that are used further to determine the resonance frequency of the edge mode (Fig. 14b). According to (32), it is $\Delta\omega^* \to \Delta\omega/(2\sqrt{2})$ for a mode with the number $s = 1$.

Topological effects manifest themselves at the boundary of the chain, where the amplitude of oscillations of the edge modes of the spin waves is maximal, and the frequency strongly depends on the configuration of the magnetization of the pillars at the edge of the chain. Moreover, the oscillation frequencies of the edge and eigenmodes differ (Fig. 14c); as a result, edge modes are localized at the chain edge, similar to the localization of edge modes of spin waves in FM films [130]. Figure 14 schematically shows the distribution of the oscillation amplitude m_i^{xy} in the chain for the main bulk (Fig. 14a) and edge (Fig. 14b) modes of spin waves at the corresponding resonance frequencies. The values for the amplitude and phase were obtained from the numerical solution of system of equations (30) for a structure of FM pillars made of permalloy in an external magnetic field $H^{ext} = 0.1$ T. Resonance frequencies for eigenmodes, $\omega_{s=1} \approx 0.7\omega_H$ and $\omega_{edge} \approx 0.92\omega_H$ for bulk and edge modes, respectively, are less than ω_H due to the nature of the dipole–dipole interaction. Similar to the edge modes, the presence of a magnetization defect (namely, the direction of magnetization in one of the pillars is opposite to that of other pillars) creates conditions for the existence of a defect vibration mode localized in the region of the defect.

The basic principle of the operation of topological magnonic devices is to create human-made magnetic structures — periodic arrays of discrete magnetic elements, domains, and domain boundaries. Such structures can be used to create waveguides, resonators, diodes, and spin wave interferometers. External effects can change in a number of cases the topology of the structures and thereby control the characteristics of the propagating spin waves.

Topological magnonic devices include systems based on nonlinear magnonic networks that enable processing information signals and implementing wave methods of data processing and logical calculations, and creating devices including those based on spin-wave interference [131–134]. The use of topological lateral microstructures [135] makes it possible to create interconnection elements in planar topologies of magnonic networks [136, 137]. It is known that the period of pumping of a spin-wave signal between lateral micro- and nanostructures can be controlled by changing the magnitude [138] and direction [139] of the external magnetic field, as well as using ferroelectric loads [140] and nonlinear effects of spin wave coupling [141]. The effects of nonlinear signal switching, which have been studied in detail in a number of physical systems, for example, in photonic waveguide structures and bound graphene layers, can also be applied in topological magnonics, since the propagation of a spin wave can locally modify the properties of an FM medium [9, 142–144]. We use the lateral system of YIG waveguides displayed in Fig. 15a as an example to explore the effects that occur during the propagation of a surface magnetostatic wave (SMSW) [9, 145] in a nonlinear regime.

A solution based on numerical simulation of the LLG equation [143, 146–148] may be used to show the spatial distribution of the dynamic magnetization component m_z for various frequencies of the input signal (Fig. 15b, d) when the input signal is applied at the left boundary of the W_1 strip. It is seen that the intensity of the output spin-wave signal (Fig. 15c, e) is distributed between ports Z_1 and Z_2. The Mandelstam–Brillouin scattering (MBS) method (referred to in English-language publications as Brillouin light scattering, BLS) may be used to observe the change in the SW propagation modes. Figure 16a, b shows maps of the spatial distribution of intensity $I_{BLS}(x, y)$ for the input-signal frequency $f_0 = 5.21$ GHz and the input signal power $P_0 = -5$ dBmW and $P_0 = 26$ dBmW, respectively. As the power of the input signal increases, the magnitude of the MBS signal at the output of the microwaveguide W_2 increases. To assess the power distribution between the output sections of both microwaveguides in qualitative terms, the coefficient $T = 10\log(S_2/S_1)$ (squares in Fig. 16f) is plotted as a function of the input power. The plot shows that the power is distributed equally between the output sections W_1 and W_2 (i.e., $T = 0$) at $P_0 = 20$ dBmW.

A phenomenological model based on the Ginzburg–Landau (GL) equations can be used to describe the dynamics

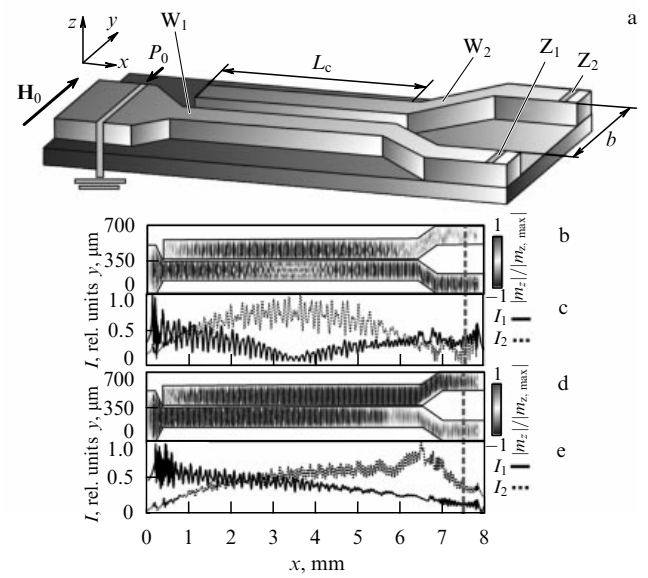

Figure 15. (a) Setup of the structure under study. Calculated spatial distribution of the dynamic magnetization component $m_z(x, y)$ (b, d) and the spin wave intensity $I(x)$ (c, e) for the input signal frequency $f_0 = 5.25$ GHz (b, c) and $f_0 = 5.36$ GHz (d, e).

of nonlinear SW propagation and coupling modes in lateral structures. The specific form of two coupled GL equations [149] can be derived from the LLG equation for dynamic magnetization with consideration for Kerr-type nonlinearity; i.e., the decrease in the saturation magnetization with an increase in the angle of deviation of the magnetization vector from that for the equilibrium state: $M \approx M_0[1 - (m_x^2 + m_z^2)/(2M_0^2)] = M_0(1 - \Phi^2/2)$, where $\Phi = [(m_x^2 + m_z^2)/M_0^2]^{1/2}$. The input power of the spin wave can be estimated in this case as $P_0 \approx |\Phi_0|^2 M_0^2 v_g w t$, where v_g is the group velocity, and $\Phi = \Phi_0$ is the initial amplitude of the SMSW for the numerical integration of the system of two GL equations:

$$\begin{cases} \mathrm{i}\,\dfrac{\mathrm{d}\Phi_1}{\mathrm{d}x} = k\Phi_1 + \chi\Phi_2 + (\zeta - \mathrm{i}v_2)|\Phi_1|^2\Phi_1 - \mathrm{i}v_1\Phi_1\,, \\ \mathrm{i}\,\dfrac{\mathrm{d}\Phi_2}{\mathrm{d}x} = k\Phi_2 + \chi\Phi_1 + (\zeta - \mathrm{i}v_2)|\Phi_2|^2\Phi_1 - \mathrm{i}v_1\Phi_2\,, \end{cases} \tag{33}$$

where $\Phi_{1,2}(x)$ is the amplitude of the spin wave in the waveguides $W_{1,2}$, $k = k(f)$ is the wavenumber of the spin wave propagating in a single microwaveguide, $\chi = \chi(f) \approx |k_s(f) - k_{as}(f)|$ is the coefficient of coupling between the spin waves, $\zeta = \partial k/\partial\Phi^2\big|_{\Phi=0}$ is a nonlinear coefficient, $f_H = \gamma H_0$, $f_M = 4\pi\gamma M_0$, and v_1, v_2 are the linear and nonlinear damping of the spin wave, respectively,

$$v_1 = \frac{1}{v_g}\left|\frac{\partial\omega}{\partial H}\right|\frac{\Delta H}{2}\,, \quad v_2 = -\frac{1}{v_g^2}\,\zeta\,\frac{\Delta H}{2}\left|\frac{\partial\omega}{\partial H}\right|\left|\frac{\partial^2\omega}{\partial k^2}\right|_{\Phi=0}\,,$$

where $\omega = 2\pi f$ is the circular frequency.

The calculation results obtained in a numerical experiment where the amplitude Φ_0 of the input signal increased show that the intensity of the spin wave in the region of the output section of the waveguide W_2 increases as a result of an increase in the coupling length of the spin waves (Fig. 16c–e). If the amplitude is further increased, the effect of nonlinear switching is observed, namely, the signal intensity is concentrated in the output section W_1. Two characteristic values of the SW amplitude may be distinguished: Φ_{th1}, at which $T = 0$

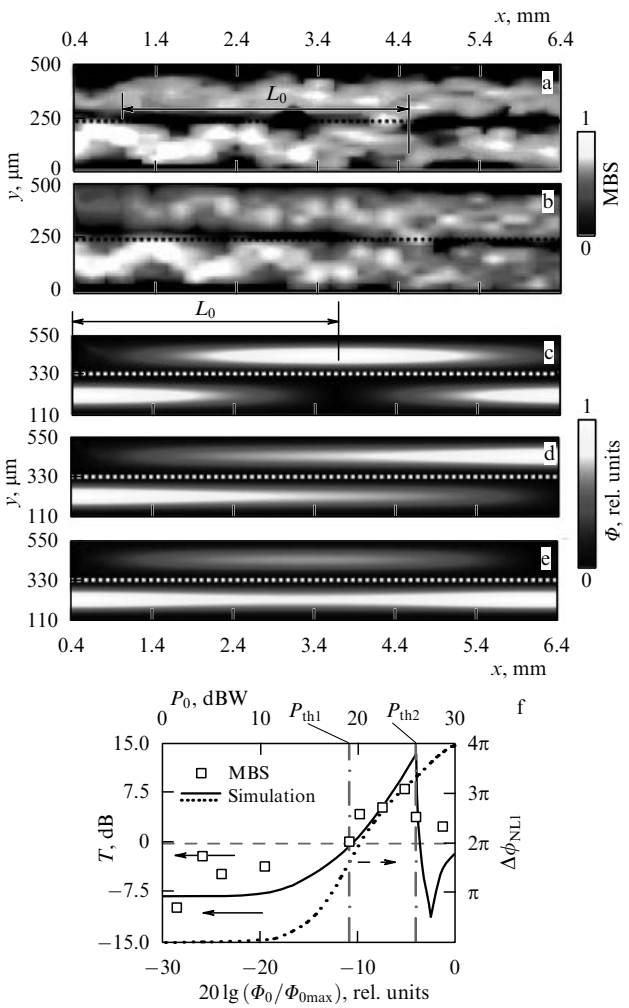

Figure 16. Spatial distribution of the MBS signal $I_{BLS}(x, y)$ at input power $P_0 = -5$ dBmW (a) and $P_0 = 26$ dBmW (b). Calculated intensity of the spin wave for the input signal amplitudes $\Phi_0 = 0.02$ (c), $\Phi_0 = 0.5$ (d), and $\Phi_0 = 0.53$ (e). (f) Coefficient T as a function of the input signal amplitude Φ_0 (lower abscissa axis) and the power of the input microwave signal P_0 (upper abscissa axis) and the nonlinear phase advance $\Delta\phi_{NL}(\Phi_0)$ as a function of the input signal amplitude.

and the signal power is divided equally between W_1 and W_2 in the output section region (Fig. 16f), and Φ_{th2}, at which the maximum possible value of the SW intensity is observed at the output section W_2. The results of a numerical calculation of the amplitude dependence of the coefficient T and the nonlinear phase advance $\Delta\phi(\Phi_0)$ [149] at the waveguide output W_1 are displayed in Fig. 16f with solid and dashed curves, respectively. Thus, nonlinear effects in magnonic microstructures may be used to create elements whose frequency-selective properties may be controlled by varying the input power level.

2.5 Multilayer magnonic heterostructures

Multilayer magnonic heterostructures, which include layers of ferroelectric and/or piezoelectric materials based on laterally connected microstructures, are a functional block for the development of interconnection elements in planar topologies of magnonic networks [1, 5, 9, 41, 137, 138, 140, 150–157]. The use of ferroelectric layers makes it possible to significantly expand the functionality of dielectric magnonic structures due to the double control of their characteristics

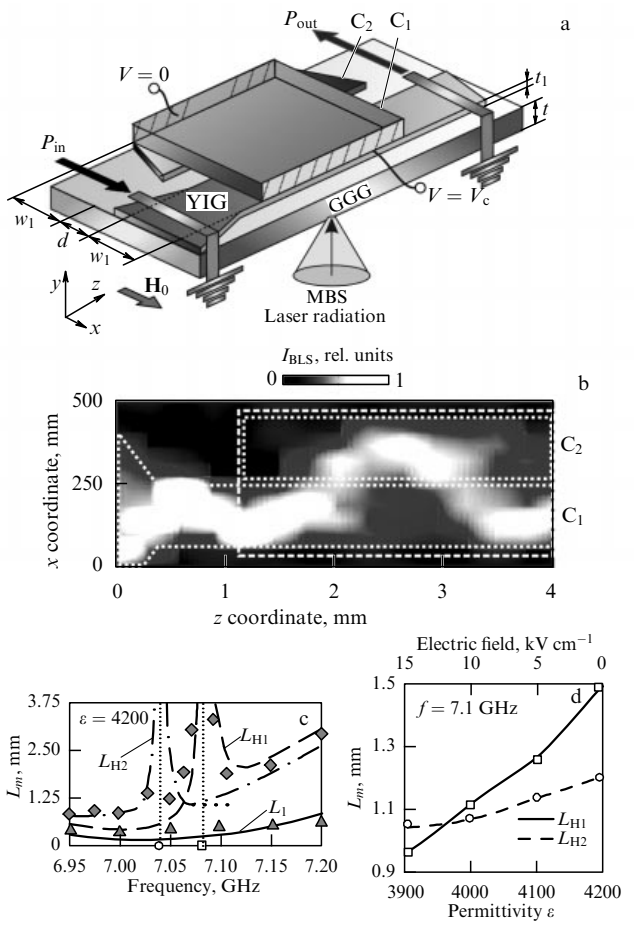

Figure 17. (a) Setup of the structure under study. (b) Measured intensity of inelastically scattered light at a frequency of 7.1 GHz. The dotted lines indicate the boundaries of the YIG strips and the FE layer. (c) Frequency dependence of the EMSW coupling length in a lateral multiferroic structure (L_{H1}, L_{H2} are calculation results, diamonds show experimental values) and lateral ferromagnetic structure (L_1 are calculation results, triangles show experimental values). (d) Coupling lengths L_m for the first and the second EMSW hybrid modes as functions of permittivity ε.

(electric and magnetic control). Control of the spectrum and spatial dynamics of hybrid electromagnetic-spin waves in a system of multiferroic microstructures with lateral spin-wave transport can be demonstrated using as an example a lateral structure, a diagram of which is shown in Fig. 17a: placed on a gallium-gadolinium garnet (GGG) substrate at distance $d = 40$ μm from each other are two YIG strips, on which a ferroelectric (FE) layer of barium-strontium titanate is located. Chromium 200-nm-thick electrodes are fixed on the edges of the FE layer. A hybrid electromagnetic-spin wave (EMSW) propagated along the parallel YIG strips in the FE layer region. A constant voltage V_c was applied to the electrodes, which made it possible to change the properties of the FE layer and, as a consequence, the EMSW characteristics.

The MBS method was used to study the spatial dynamics of EMSW in a structure with lateral spin-wave transport. The intensity I_{BLS} of the optical signal turns out to be proportional to the square of the dynamic magnetization in the spatial region where the laser beam is focused on the back surface of the YIG film in a backscattered configuration.

The experimentally observed distribution of the EMSW intensity in the structure with lateral spin-wave transport, which was obtained by the MBS method, is displayed in Fig. 17b, where shades of gray indicate the EMSW intensity $I_{BLS}(x, z)$ at an input signal frequency $f_{el} = 7.1$ GHz. These data may be used to determine the coupling length that is equal to the distance along the z axis at which the wave energy is pumped from the first YIG strip to the second one. Figure 17c shows the frequency dependence of the coupling length for the first (L_{H1}) and second (L_{H2}) EMSW eigenmodes. If the FE layer is absent (L_1 in Fig. 17c), the coupling length increases monotonically with increasing frequency at $f > 7.04$ GHz. If the FE load is applied at a frequency lower than the frequency of the transverse ferromagnetic resonance (FMR), the lengths of coupling of one microwaveguide to another increase sharply for both the first and second modes. This is explained by the intersection of the dispersion characteristics of the symmetric and antisymmetric EMSW modes (the corresponding frequencies are indicated by the square and circle in Fig. 17c). Thus, the FE layer may be used to control the coupling length of the higher modes of the layered structure.

Figure 17d shows the calculated variation of the coupling length as a function of the dielectric constant of the FE layer for the frequency $f = 7.1$ GHz for the first and second modes of the hybrid wave. It can be seen that the coupling length L_{H1} of the first hybrid mode increases as ε grows faster than that for the second mode L_{H2}. As shown in Ref. [138], the pumping length can be controlled by varying the applied magnetic field, and since the dielectric constant of the FE layer changes when an external constant electric field is applied, the proposed multiferroic structure can be used as a power coupler with double control and selection by the transverse mode type, given that $|\mathrm{d}L_{H2}/\mathrm{d}E| < |\mathrm{d}L_{H1}/\mathrm{d}E|$.

3. Experimental methods for studying dielectric magnonic structures

The variety of properties of magnetic materials and dielectric magnonic structures created on their basis necessitates the use of a comprehensive approach to experimental studies of the static and dynamic magnetic properties of the structures carried out in a wide range of magnetic fields and various frequency ranges. At present, several basic experimental methods are used in conjunction in studying magnonic structures to determine both the magnetic characteristics of the original materials and the features of the spectra of spin-wave excitations.

The ferromagnetic resonance method is widely used to determine the magnetic characteristics of materials. The FMR phenomenon [158, 159] consists of the resonance absorption of a high-frequency electromagnetic field by a magnetic medium. The theoretical foundations of the FMR method and methods of its practical implementation are described in many papers [9, 160, 161]. The classical FMR method based on a microwave resonator assumes that the magnitude and direction of the external magnetic field are varied at a fixed frequency of the microwave signal ($f \approx 10$ GHz). Resonance magnetic fields $\mathbf{H}_r$ at a given direction of magnetization are determined from the maxima of the power absorbed by the magnetic specimen. The fields $\mathbf{H}_r$ may correspond in the general case to both homogeneous and nonhomogeneous modes (spin-wave resonances) of oscillations of the magnetization in the specimens. An analysis of FMR spectra provides information on the main characteristics of spin systems: saturation magnetization, the

FMR linewidth, relaxation times, exchange interaction and magnetic anisotropy constants, the degree of spin pinning at the boundaries of magnetic layers, etc. [162–167]. The FMR method is widely used at present to characterize nanometer films of magnetic dielectrics [168, 169], multilayer magnetic structures grown on dielectric [170] and semiconductor (GaAs, Si) [171] substrates, and magnetic films in a multidomain state [172–176].

The expansion of magnonic devices to the range of micrometer and sub-micrometer geometric dimensions and the need for an experimental study of spin dynamics (spin transfer, spin Hall effect, spin oscillators, etc.) in magnetic structures at various time and spatial scales led to the development of the so-called broadband FMR method [177–180]. The broadband FMR method enables exploration of homogeneous and inhomogeneous modes of magnetization oscillations in magnetic structures in various modes in a setup where the value of the external static magnetic field is fixed while the frequency of the dynamic magnetic field is varied, and vice versa. The broadband FMR method is based on the measurement of the microwave power absorbed by magnetic structures placed in microresonators or regular transmission lines. Measurements are carried out using vector network analyzers (VNAs), employing sections of microstrip or coplanar waveguides as transmission lines. In contrast to the classical FMR, this method allows conducting measurements in a wide frequency range, from hundreds of MHz to dozens of GHz. This method was used, for example, to study spin dynamics at low frequencies [181] and in nanosized magnetic elements [182], to measure the exchange constant in YIG [183], and to investigate characteristic frequencies of spin oscillations in layered ferromagnetic semiconductor structures.

In developing magnonic signal processing devices, the FMR method and its modifications are usually used at the initial stages to determine the magnetic characteristics of materials and structures. Although the FMR method can be applied to characterize magnonic devices, for example, filters [184], a method based on the measurement of S-matrix elements is widely used in the microwave range of radio waves. The method for measuring S-matrices of magnonic devices, like the broadband FMR method, is based on the use of VNAs and microwaveguides. However, to generate and detect spin-wave excitations in magnetic structures, spatially separated antennas are used, the role of which is performed by sections of microstrip or coplanar waveguides formed both on dielectric substrates and on the surface of magnetic structures. The measured frequency characteristics of the S-matrix elements can be used to determine the amplitude and phase frequency characteristics of the device, group delay time, dispersion characteristics of spin waves, resonant oscillation frequencies, dissipative parameters, etc. This method, which is quite flexible and relatively simple to implement, is based on the functionality of standard VNAs; it is used, for example, in magnonics to study magnonic crystals [185], spin waveguides [186], interferometers [187, 188], directional couplers [138], ferrite-semiconductor structures [189], etc.

A disadvantage of this method is the need to eliminate parasitic crosstalk between spin antennas in electromagnetic fields, which reduces the dynamic range and sensitivity of measurements in the microwave range of radio waves.

To study the space–time dynamics of spin-wave excitations in magnetic media and magnonic devices, optical probe methods are widely used, one of which is based on the Mandelstam–Brillouin scattering of light [190, 191]. The theoretical foundations of the MBS effect in magnetically ordered media are presented in a large number of studies [192–195]. The MBS method based on the use of a multipass Fabry–Perot interferometer [196] is characterized by the following basic parameters: the measurement range of the frequency characteristics of scattered optical radiation is 1–100 GHz, the time resolution is as high as to 1 ns, and the spatial resolution is 10 μm. Modifications of the MBS method have been proposed that provide phase and wavenumber resolution with a spatial resolution up to 250 nm [197–200].

To date, an immense number of studies have been carried out to explore, using the MBS method, various aspects of spin dynamics in magnetic structures and magnonic devices (see, in particular, [195, 201]). It should be noted that the MBS method is often employed in combination with FMR methods and VNA-based measurement methods [5, 202, 203].

4. Magnonic crystals

Human-made magnetic materials, known as magnonic crystals (MCs), whose properties periodically change in space, are very promising candidates for controlling and manipulating magnetic excitations. Magnonic crystals are a magnetic analogue of photonic, phononic, and plasmonic crystals. A fundamental feature of periodic structures, including MCs, is the presence of Bragg resonances, which result in the emergence (in the spin wave spectrum) of bandgaps for wavenumbers satisfying the Bragg condition.

To date, extensive studies of MCs have been carried out, in which the periodicity was created in various ways. Static MCs are known that are created, for example, by modulating the geometric parameters of a ferromagnetic film (thickness, width), using periodic boundary conditions (in the form of metal or ferroelectric semiconductor lattices on the ferromagnetic film surface), the formation of holes, and layers of various magnetic materials. Dynamic MCs, in which a periodic magnetic field and electrically controlled periodicity are created; tunable MCs formed by a periodic system of strips magnetized in the same direction or in opposite directions on an FM film surface; MCs with temperature periodicity created by laser irradiation; and moving MCs, in which periodic strains are created by an acoustic wave propagating in an FM film, are all well known.

It was proposed to control the characteristics of the bandgaps in an electric and magnetic way by violating the periodicity and creating defects, changing the power of the input signal, etc. The presence of bandgaps opens up wide possibilities for using MCs in microwave devices for functional processing of signals carried by spin waves, including in microwave filters, in microwave signal generators based on self-oscillating ring systems, and for frequency inversion and time reversal, data buffering, etc. [8].

Crystals made from YIG FM films feature broad capabilities; however, their efficiency is limited by losses. The control of spin waves with low losses in an MC consisting of nanosized YIG strips was experimentally demonstrated in [204]. Amplification of spin waves in the allowed transmission bands is achieved by filling the gaps between the YIG strips with CoFeB layers. The MCs formed in this way have tunable bandgaps 50–200 MHz wide with almost complete suppression of the spin-wave signal. Bragg

scattering on even two YIG strips was shown to yield clearly distinguishable bandgaps in the transmission spectra of spin waves. Thus, the integration of ferromagnets with a high saturation magnetization into YIG-based nanosized MCs provides efficient processing of spin waves and low-loss propagation, which is of importance for magnonic technologies.

Study [205] explored a 1D MC based on a 10.2-μm-thick YIG film with a periodic system of eight Cu strips on its surface. To exclude edge reflections, absorbers made of a 30-nm-thick Au film located at the MC ends were used. A magnon bandgap for direct bulk magnetostatic waves, which was observed near the frequency of 1.80 GHz, had a depth of −4.6 dB, a value that agrees well with simulation results. The characteristics obtained over the past several years in the study of MCs in a number of papers are illustrated by the plot of the depth and width of bandgaps as a function of the number of periodic inhomogeneities.

The results of studies of 2D MCs that consist of one- and two-component arrays of interacting magnetic points or lattices of holes (anti-dots) using MBS technology are analyzed in [206]. In particular, the main properties of the band diagram of such systems have been considered, with special attention paid to its dependence on both magnetic and geometric parameters. Owing to the possibility of the band structure being changed using several degrees of freedom, planar 2D MCs open up prospects for the development of nanoscale microwave devices.

The propagation of inverse bulk and surface magnetostatic spin waves in a 1D MC with a system of grooves on the surface under the effect of a continuous spatial temperature gradient was studied [207]. A thermal gradient applied along the direction of wave propagation was shown to result in a shift in the bandgap frequency and a change in the transmission characteristics of spin waves. The frequency shift is caused by saturation magnetization being altered due to the change in absolute temperature. The change in the transmission characteristics, which is exhibited in broadening the MC bandgap, is the result of the spatial transformation of the spin wavelengths in the thermal gradient. The transmission characteristics of spin waves in a thermal gradient are numerically calculated based on the transmission matrix approach.

Experimental studies of the effect of magnetic crystallographic anisotropy on the parameters of dynamic MCs that emerge during the propagation of surface acoustic waves (SAWs) in YIG films are presented in [208]. The main features of this effect include: (1) the emergence of additional bandgaps together with the main magnon bandgap that exists without anisotropy, (2) the absence of reflections of the incident surface magnetostatic wave at frequencies of additional bandgaps, and (3) the feasibility of achieving the same depth of additional bandgaps at a relatively low power of SAWs, almost an order of magnitude smaller than in the case of the main bandgaps. A possible explanation for these features is given in terms of inelastic scattering of surface magnetostatic waves using a SAW with the transformation of the reflected surface wave into an anisotropic direct bulk magnetostatic wave, the existence of which is due to cubic crystallographic anisotropy in the YIG.

A 3D model of periodic meander-shaped FM films is presented in [60]. The propagation of spin waves in such films and vertically coupled structures was studied using micromagnetic simulation and the plane wave method. Spin waves

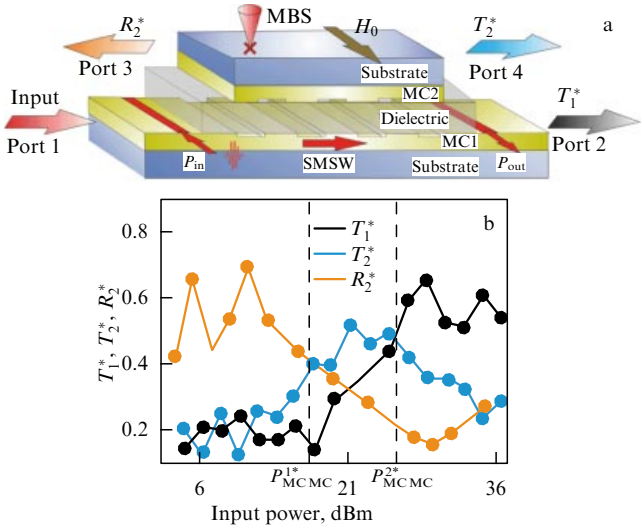

Figure 18. (Color online.) (a) Layered MC1/MC2 structure. T_1^*, T_2^*, R_2^* are transmission factors. (b) Transmission factors for port 2 (black curve), port 3 (orange curve), and port 4 (blue curve) as functions of the input signal power.

in these structures mainly propagate in film segments oriented at right angles to each other. Owing to this feature, the wave can propagate in three dimensions. The internal effective magnetic fields and the dispersion of spin waves in single and vertically coupled structures have been calculated. A comparison of the propagation of surface and bulk spin waves in such meander films has been carried out.

Figure 18a shows a composite structure based on two coupled MCs separated by a dielectric layer (MC1 (YIG)/MC2(YIG)). MC1 and MC2 are 12-μm-thick YIG films on GGG substrates, on the surface of which a periodic system of grooves with a period of 200 μm and a depth of 1 μm was created. A 50-μm-thick mica plate was used as a dielectric. The operating frequency was chosen in the center of the bandgap of the structure. The periodic alternation of intensity maxima and minima in such a structure, in contrast to that in the YIG1/YIG2 structure, only occurs in a certain range of input signal power.

We choose an observation point at the maximum of the signal in MC2, for example, at a distance of $l = 3\lambda/2$ from the entry. The transmission characteristics of each of the output ports for such a structure are plotted for this section; they are displayed in different colors in Fig. 18b. There are two threshold values of power, P^{1*}_{MCMC} and P^{2*}_{MCMC}, at which the dynamics of the system alters. Three areas may be distinguished: at low input power, most of the signal exits through port 3, at high input power, through port 2, and at medium power, through port 4. Thus, if the signal is output from port 3, the structure operates as a power limiter; if from port 2, as a suppressor of weak signals; and if from port 4, a signal of a medium power level can be separated. If a signal is output from all ports, the MC1(YIG)/MC2(YIG) structure enables spatial separation of signals of different power levels across the ports of the structure.

Research is also being actively carried out at present aimed at determining the feasibility of using the nonlinear properties of systems with lateral and vertical spin-wave transport [5, 134, 141, 209, 210]. The development of technologies for the production of 1D and 2D MCs based on YIG films enables the creation of magnetically tunable

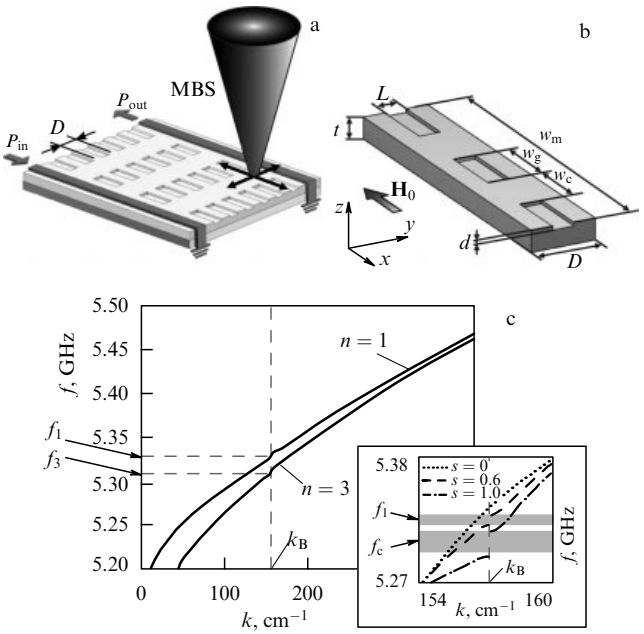

Figure 19. (a) Schematic representation of the structure under study in a configuration with three waveguide channels. (b) Setup of a unit cell of a magnonic-crystal structure used in numerical simulation by the finite element method. (c) Dispersion characteristic of modes ($n = 1$, $n = 3$) of the magnonic crystal structure with coefficient $s = 0.6$. The inset shows the dispersion characteristics of the lowest waveguide modes at $s = 0$ (dotted curve), $s = 1$ (dashed-dotted curve), and $s = 0.6$ (dashed curve).

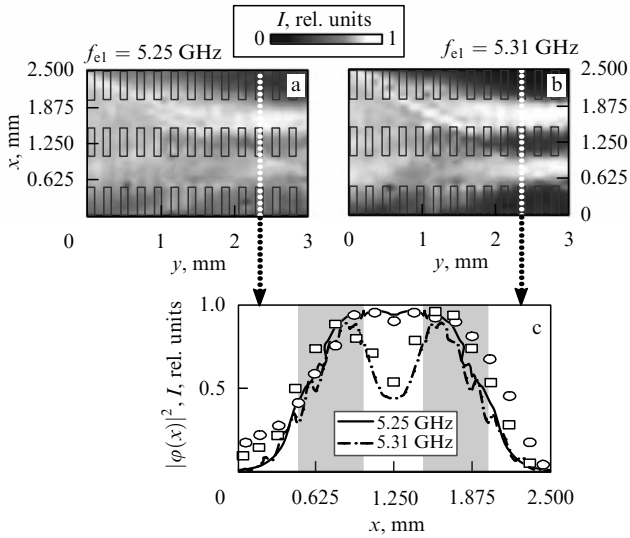

Figure 20. (a) Map of the distribution of the spin wave intensity in the structure under study at a frequency of $f_{e1} = 5.25$ GHz. (b) Map of the distribution of the spin wave intensity in the structure under study at a frequency $f_{e1} = 5.31$ GHz. (c) Distribution of the internal field of the first mode in the studied magnonic-crystal structure along the x axis for frequencies of 5.25 GHz (solid curve — calculation results, ovals — experimental values) and 5.31 GHz (dashed-dotted curve — calculation results, squares — experimental values). The gray-shaded areas correspond to the position of channels with width w_c on the surface of the YIG film.

devices for generating, processing, and transmitting signals in the microwave range, such as super-high frequency filters, phase shifters, couplers, data storage devices, sensors, high-speed switches, and magnonic-logic devices [1, 136–138, 156, 211, 212]. An important issue that arises in this case is how to determine the mechanisms that control the spatial-frequency selection of spin waves propagating in the magnonic crystal structure [212, 213]. We now consider the specific features of the formation of waveguide channels using as an example a structure that is a 2D magnonic-crystal lattice (Fig. 19).

The spectrum of magnetostatic eigenwaves in transversely bounded regular ferrite waveguides is known to be discrete and consist of a set of SMSW modes with different field distributions over the waveguide width (width modes). If a certain periodic system is located on the surface of waveguides, (Bragg) bandgaps emerge in such structures, which is a property characteristic of MCs. Figure 19c shows the dispersion characteristics of the first and third width modes of the SMSW ($n = 1$ and $n = 3$) [214, 215] of the structure under study. It can be noted that, at the value of the wavenumber $k = k_B = \pi/D = 157\ \text{cm}^{-1}$, the dispersion characteristics exhibit bandgaps with frequencies $f_1 = 5.325$ GHz and $f_3 = 5.31$ GHz for the first and third mode, respectively. The inset in Fig. 19c shows the calculated dispersion characteristics of the lowest SMSW modes ($n = 1$) for various values s of the filling factor for a magnonic-crystal waveguide as the ratio of the total width of all grooves to the waveguide width w_m. It is seen that, as s decreases, the frequency width of the bandgaps decreases. In the case of the magnonic crystal lattice under study ($s = 0.6$), the bandgap with the central frequency $f_1 = 5.325$ GHz narrows to $\delta f_1 = 5.327 - 5.324 = 3$ MHz, which is clearly seen in the enlarged part of the dispersion characteristics in the region of frequencies f_1 and f_c and wavenumber k_B displayed in the inset in Fig. 19c. A decrease in the filling factor s leads to weakening of the coupling of the direct and inverse waves, i.e., waves that propagate along the positive and negative directions of the y axis, respectively, which, in turn, results in a decrease in the frequency width of the bandgap.

An experimental study of the dynamics of SMSW propagation in the structure under consideration was carried out by the MBS method. The measured intensity of the optical signal I is in this case proportional to the square of the dynamic magnetization in the region where the laser beam is focused on the YIG film surface.

Figure 20a shows the SMSW intensity distribution $I(x, y)$ for the input signal frequency $f_{e1} = 5.25$ GHz. The black rectangles indicate the groove areas on the surface of the YIG film. Since this frequency is far from the Bragg resonance frequency, the effect of the periodic system on the surface of the YIG film on the dispersion characteristics and the transverse distribution of the mode amplitudes is virtually absent. The spatial distribution of the dynamic magnetization squared corresponds in this case to the result of the interference of the first and third width modes [214, 215] of a YIG waveguide with width w_m. If the frequency of the input signal corresponds to that of the third mode bandgap f_3, namely $f_{e2} = 5.31$ GHz (Fig. 20b), the distribution of the SMSW intensity in the structure under study changes. A redistribution of the SMSW is observed, namely, intensity maxima emerge in the intervals between the periodic structures, i.e., in areas with constant film thickness.

Figure 19c shows that this frequency lies within the third mode bandgap ($n = 3$); thus, this mode is strongly attenuated during propagation through the periodic system of grooves, while the first mode ($n = 1$) makes the main contribution to the observed distribution of intensity. The concentration of the SMSW intensity in the region of the structure, where there

is no periodic system of grooves on the YIG surface, is only observed at frequencies close to the frequency f_3, which indicates the connection of this effect with the transformation of the eigenmodes of the structure in the frequency region of the Bragg bandgap. Figure 20c displays the profile of the first mode of the SMSW (dashed-dotted curve) that propagates in the structure under study. At the same time, the wave that corresponds to the third mode is attenuated due to the bandgap condition in effect. The experimental results are presented in Fig. 20c for 5.25 GHz (ovals) and 5.31 GHz (squares). Good agreement with the numerical simulation is seen. Thus, waveguide channels in a magnonic-crystal structure may be formed when the frequency of the input signal coincides with that of the bandgap.

5. Ferrite–semiconductor magnonic waveguide structures

Semiconductor electronics based on 'metal–insulator–semiconductor' (MIS) structures [216] provide high-speed performance of functional elements with low power consumption and heat release. However, as the size of the elements decreases, fundamental physical limitations come into play, which are associated with a change in the dielectric and conductive properties of semiconductors and dielectrics on nanometer spatial scales. Other limiting factors are heat release and an increased density of heat fluxes due to the flow of electric currents in the MIS structures. An alternative approach that can overcome the above limitations is to use spins or magnons (spin waves) as information carriers [110, 142, 217].

An important step towards combining the elements of magnonics and semiconductor electronics is to integrate magnetic structures, which effectuate spin transfer, with existing semiconductor functional elements, which implement electron transfer. To solve this problem, it is necessary, first of all, to select the appropriate combinations of magnetic and semiconductor structures and their material parameters.

Magnetic structures based on single-crystal YIG films, which are characterized by record-setting low losses in SW propagation and high ohmic resistance, are promising candidates for such integration. However, the incorporation of magnonic YIG elements into semiconductor electronics encounters a number of problems. Notably, one problem is that semiconductor substrates and single-crystal magnetic films are not compatible in either the parameters of their crystal lattices or the temperature regimes of their growth. Monocrystalline and polycrystalline YIG films are usually grown on GGG substrates by liquid-phase epitaxy, magnetron sputtering [218], ion-beam sputtering [171], or pulsed laser deposition [219]. In semiconductor electronics, especially in creating devices for the microwave range of radio waves, substrates based on gallium arsenide (GaAs) are widely used, which feature a high mobility of charge carriers (the mobility of electrons and holes is 8600 cm^2 $(V\ s)^{-1}$ and 400 cm^2 $(V\ s)^{-1}$, respectively) and a wide bandgap $\Delta\varepsilon = 1.42$ eV [220]. Thus, magnetic structures based on YIG films combined with GaAs substrates (ferrite–semiconductor structures) are promising candidates for integrating magnonics and spintronics elements into existing and future semiconductor technologies.

Another challenging task is to develop adequate methods for characterizing the resulting ferrite–semiconductor structures in terms of both the material parameters of the layers (saturation magnetization, characteristics of crystallographic anisotropy) and their high-frequency properties (characteristic frequencies of spin-wave excitations, dissipative parameters, etc.) in a wide range of magnetic fields and frequencies.

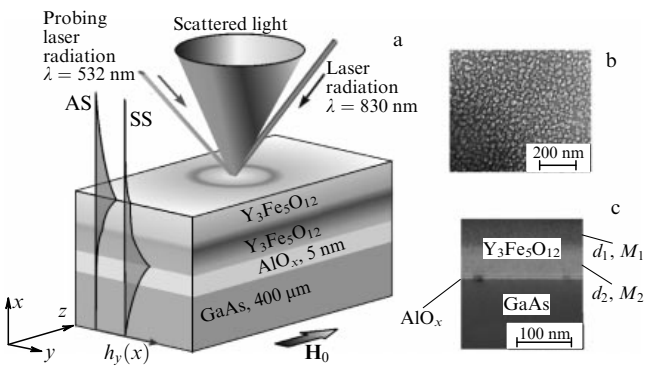

Figure 21. (a) Schematic representation of the YIG/GaAs structure and configuration of the MBS method. Micrograph of the surface of the structure (b) and cross section of the structure (c).

This section presents the results obtained in the development of a technology for the production of YIG/GaAs layered structures and the characterization and investigation of spin-wave excitations in such structures by the FMR method and the MBS method [221, 222].

A semi-insulating n-GaAs substrate with orientation (100) and a thickness of 400 μm was used as a semiconductor base. A YIG film was deposited onto the substrate using ion-beam sputtering in an Ar^+O_2 atmosphere [171]. To reduce the elastic deformation of the lattice and diffusion into the YIG layer of Ga and As ions, a 4-nm-thick AlO_x layer was sputtered. Next, to match the constants of the crystal lattices, a YIG buffer layer was sputtered. The second YIG layer was sputtered after planarization and annealing. A general diagram of the resulting structure, the sequence of the layers, and micrographs of the surface and cross section are displayed in Fig. 21. The results of the studies showed that the obtained YIG layers have a polycrystalline structure with grain sizes varying from 20 to 60 nm and a total thickness $d_1 + d_2$ of about 100 nm.

The FMR spectrum was measured by the resonator method in a magnetic field range from 0.1 to 5.5 kOe at fixed frequency $f_r = 9.87$ GHz and two orientations of the external magnetic field: in the plane of the structure ($H_\parallel$) and perpendicular to the plane ($H_\perp$). The response of the magnetic structure, which was observed for any orientation of the magnetic field, exhibited two values of the resonance magnetic fields H_{ri} ($i = 1, 2$ is the sequential number of the resonance for a given orientation r of the external magnetic field) that correspond to homogeneous modes of magnetization precession in the layers.

The results of measuring the resonance fields are presented in the table. The effective magnetization values of each layer for each orientation were estimated as

$$4\pi M_\perp = H_r - \frac{f_r}{\gamma}\,, \quad 4\pi M_\parallel = \frac{(f_r/\gamma)^2 - H_r^2}{H_r}\,, \tag{34}$$

where $\gamma = 2.8$ GHz kOe^{-1} is the gyromagnetic ratio.

Thus, the following conclusions can be drawn from the results obtained by the FMR method for the structure under

Table. Measurement results.

Parameter	Orientation $H_{\parallel}$	Orientation $H_{\perp}$
Resonant magnetic field, kOe	$H_{\parallel 1} = 2.895$, $H_{\parallel 2} = 3.001$	$H_{\perp 1} = 4.882$, $H_{\perp 2} = 4.707$
FMR line width, Oe	$\Delta H_{\parallel 1} = 223$, $\Delta H_{\parallel 2} = 134$	$\Delta H_{\perp 1} = 52$, $\Delta H_{\perp 2} = 198$
Effective magnetization, kG	$4\pi M_{\parallel 1} = 1.397$, $4\pi M_{\parallel 2} = 1.139$	$4\pi M_{\perp 1} = 1.357$, $4\pi M_{\perp 2} = 1.182$

study and their comparison to the material parameters for pure single-crystal YIG (saturation magnetization $4\pi M_0 = 1.750$ kG, FMR line width 0.5–1 Oe): the YIG layers grown on the GaAs substrate have a lower saturation magnetization and a wider FMR line than does pure YIG; the saturation magnetizations of the layers differ significantly; the films are sufficiently homogeneous regarding magnetic parameters, and inhomogeneous modes of magnetization precession are not observed. Such differences in the saturation magnetization and FMR linewidth of the magnetic structure are due, in our opinion, to the effect of the growth anisotropy and the polycrystalline structure of the obtained YIG layers. Since the FMR method does not enable association of the obtained magnetization values with a specific magnetic layer, it was further assumed that the lower magnetization value corresponds to the upper YIG layer of thickness d_1 (Fig. 21c), i.e., $4\pi M_1 = 1.139$ kG (for a layer with d_2, $4\pi M_2 = 1.397$ kG).

The spectra of spin-wave excitations in the YIG/GaAs structure were further investigated by the MBS method, which makes it possible to measure the characteristics of both coherent and incoherent ('thermal') spin waves in a frequency range of 1–100 GHz. The MBS spectra of incoherent SWs in a frequency range of up to 20 GHz at various values of the external magnetic field are shown in Fig. 22a. At a given value of the external magnetic field, the spectral peaks with the lowest frequencies in the Stokes and anti-Stokes spectral regions (designated in Fig. 22a as SS (Stokes spectrum) and AS (anti-Stokes spectrum), respectively) belong to the lowest SW modes that propagate along the positive and negative directions of y. The rest of the spectral peaks correspond to the frequencies of the perpendicular standing spin wave (PSSW) resonances [223] in a structure with two YIG layers with different thicknesses and magnetizations. These peaks are designated in Fig. 22 as PS_{nl} and PA_{nl} for the Stokes and anti-Stokes parts of the spectrum (n is the PSSW mode number and $l = 1, 2$ is the number of the magnetic layer with magnetization M_l). In the case of free spins and the absence of interlayer exchange interaction, the dispersion characteristics of the highest modes ($n > 0$) of dipole-exchange waves in an isolated magnetic layer are given by the expression [224]

$$\omega_{ln} = \sqrt{\omega_{lnk}(\omega_{lnk} + \omega_{Ml})}\,, \tag{35}$$

where $\omega_{ln} = 2\pi f_{ln}$ is the angular frequency, $\omega_{lnk} = \omega_H + q\omega_{Ml}(k^2 + (n\pi/d_l)^2)$, $q = 3 \times 10^{-12}$ cm^2 is the constant of inhomogeneous exchange [224], and k is the longitudinal wavenumber of the SW. Equation (35) at $k = 0$ may be used to determine the PSSW resonance frequencies. The measured PSSW resonance frequencies and the known values of the layer magnetizations in Eqn (35) may be used to determine the thickness of each YIG layer. Figure 22b displays the experimental field dependences of the PSSW frequencies PS_{nl} and theoretical curves plotted using Eqn (35) for YIG layer thicknesses $d_1 = 54$ nm and $d_2 = 60$ nm. It is seen that the experimental and theoretical results for the PSSW frequencies are in good agreement with each other. The same figure shows the field dependences of the lowest SS modes of spin waves.

However, experimental studies by the MBS method carried out with a better frequency resolution revealed that the SS peak splits into two, and the degree of frequency splitting of the peaks depends on the direction of magnetization of the YIG/GaAs structure along the positive or negative direction of the z axis (see Fig. 21). Thus, the characteristics of propagation of the lowest SW modes are nonreciprocal. The nonreciprocity of propagation inherent in surface spin waves arises, for example, when the symmetry of the boundary conditions on the surfaces of the YIG layer is violated due to the metallization of one of the surfaces. For instance, a dispersion equation is presented in Ref. [225] in the dipole approximation for a two-layer YIG structure, taking into account the finite conductivity σ of the GaAs layer. The conductivity σ of the GaAs layer may be controlled, for example, by irradiating its surface with light whose photon energy E_f is greater than the width of the GaAs bandgap $\Delta\varepsilon$ and sufficient to inject electrons from the valence band into the conduction band.

The dispersion characteristics of SWs and the phenomenon of nonreciprocity in the YIG/GaAs structure were

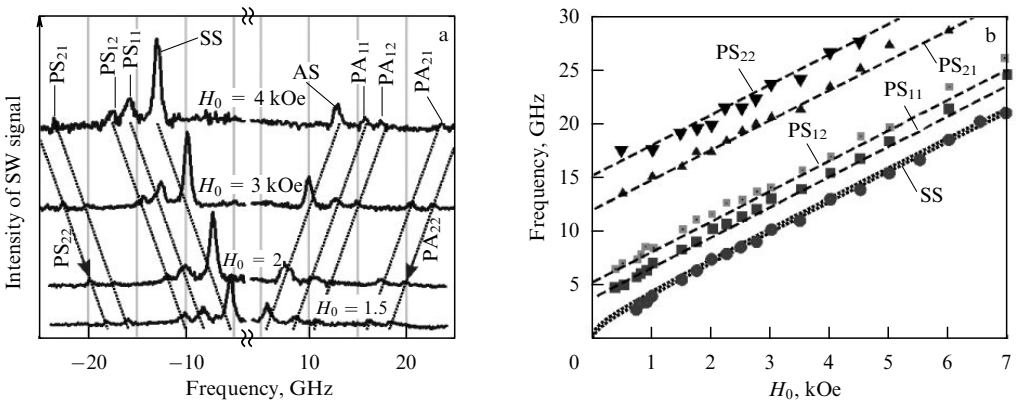

Figure 22. (a) MBS spectra of incoherent spin waves in a YIG/GaAs structure obtained at different values of the external magnetic field. (b) Field dependences of the resonance frequencies of a PSSW with $n = 0$ — filled circles, $n = 1$ — filled squares, and $n = 2$ — filled triangles. Dashed lines represent the frequencies calculated using Eqn (35).

studied using the MBS method with wavenumber selection [222] in two cases: with and without exposure to infrared (IR) radiation of the GaAs surface from the YIG side. A semiconductor laser with a wavelength $\lambda = 830$ nm and a radiation power of 5 mW, which was focused onto a region 1 mm in diameter on the surface of the structure, was used as a radiation source. The dispersion characteristics of the SW were measured in the same region at a fixed value of the external magnetic field $H_0 = 2$ kOe. The experimental and theoretical results are displayed in Fig. 22. It is seen that the dispersion characteristics of the highest SW modes and the resonance frequencies of the PSSW do not depend on the direction of magnetization of the structure or irradiation of its surface. Good agreement is observed for this part of the SW spectrum between the experimental results and theoretical calculations of the SW dispersion and PSSW frequencies using Eqn (35). The independence of the characteristics of higher SW modes on the magnetization direction and the exposure to IR radiation is explained by these characteristics being primarily determined by the state of the spins on the surface of the YIG layers (free, fixed, etc.), rather than by the conductivity properties of the GaAs substrate.

We now consider the lowest SW modes (the AS and SS branches) (Fig. 23) and the corresponding experimental points of dispersion characteristics obtained without and under the effect of radiation. Regardless of the direction of SW propagation, two branches of the dispersion characteristics of the lowest SW modes are observed: high-frequency and low-frequency. We distinguish two ranges of wavenumbers: $0 < |k| < 3$ μm^{-1}, the region of 'small' wavenumbers, and $3 < |k| < 15$ μm^{-1}, the region of 'large' wavenumbers. In the region of negative wavenumbers, the position of the experimental points on both branches of the dispersion characteristics is virtually independent of the irradiation effect. It should be noted that the experimental points on the high-frequency branch are located in the region of small wavenumbers, while on the low-frequency branch, they are in the region of large wavenumbers.

In the case of positive wavenumbers, exposure to radiation leads to an upward frequency shift of the experimental points only in the region of small wavenumbers and on the high-frequency branch. The frequency shift of the order of 220 MHz is due to the increase in GaAs conductivity under the effect of irradiation.

To provide a qualitative explanation of the observed patterns displayed in Fig. 23, the theoretical dispersion characteristics obtained at various approximations are introduced. Solid curves show the dispersion characteristics of dipole (magnetostatic) waves in the investigated two-layer YIG structure [225], loaded from the side of the layer with thickness d_2 by a GaAs semiconductor substrate with conductivity $\sigma = 10^7\ \Omega^{-1}$. Calculations have shown that the effect of conductivity on the characteristics of dipole waves (an increase in the frequency of dipole waves at a fixed value of the wavenumber) is only exhibited in the YIG/GaAs structure in the region of small positive wavenumbers related to the high-frequency branch of the dispersion curve. An analysis of the distribution of the components of high-frequency magnetic fields over the thickness of the two-layer structure has shown that the spin wave is localized under these conditions at the interface between the YIG-d_2 layer, and GaAs and its fields effectively interact with GaAs conduction electrons. In other cases, SWs are localized at the boundaries opposite to the GaAs layer.

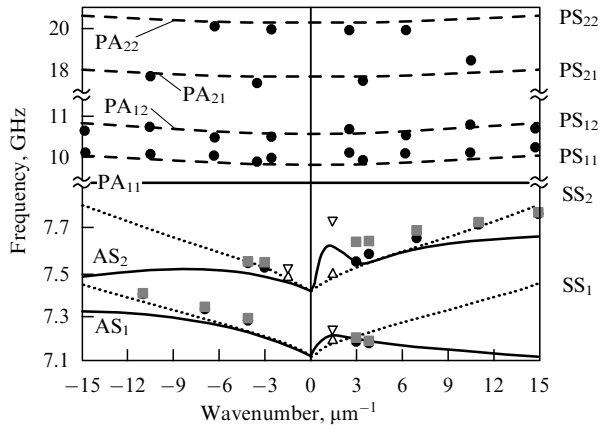

Figure 23. Dispersion characteristics of an SW for YIG/GaAs in an external 2-kOe field without IR radiation (dots and upward facing triangles) and with IR radiation (filled squares and downward facing triangles). The dashed lines show the result of calculations for PSSW modes using Eqn (35). Solid curves are calculated using the dispersion equation [225], while dashed curves were obtained using the equation for dipole-exchange waves [224].

It should be noted that the simplified approach proposed in [225] does not provide a quantitative estimate of the frequency shift of the dispersion characteristics. To obtain a quantitative estimate, it is necessary to solve the more rigorous problem of the interaction of radiation with a semiconductor layer and the generation of charge carriers.

The dipole approximation becomes inapplicable in the region of large wavenumbers ($|k| > 3$ μm^{-1}). Dashed lines in Fig. 23 show the dispersion characteristics of the lowest ($n = 0$) dipole-exchange SW modes [224] in isolated YIG films with thicknesses d_1, d_2 and magnetizations M_1, M_2. The dispersion characteristics of the dipole and dipole-exchange waves virtually coincide in the region of small wavenumbers at conductivity $\sigma = 0$.

Thus, it was shown in this section that the dispersion characteristics of spin waves in thin YIG films on GaAs substrates can be varied in a controlled manner using optical radiation. In particular, the IR-induced change in GaAs conductivity results in the spin wave frequency being shifted by up to 220 MHz. The radiation-induced nonreciprocity effect in a two-layer YIG film is described on the basis of a simple analytical theory. The research results can be used to integrate magnonic devices into semiconductor electronics.

6. Domain walls and skyrmions in magnonic devices

The walls between magnetic domains can feature a variety of substructures. For example, already the first realistic model of the domain structure developed by Landau and Lifshitz [146] contained 90-degree walls between strip and closure domains and 180-degree walls between strip domains. Bloch, Néel, twisted domain walls, and their numerous varieties are effectuated, depending on the parameters and dimensions of the magnetic material and the parameters of the external effect [110, 226–229]. The width of the domain wall (DW) can usually vary from several nanometers to several dozen nanometers. Domain walls, owing to their dimensions in combination with their capability to move, are mobile nano-objects attractive as candidates for the development of reconfigurable spintronic and magnonic devices with nano-

meter-sized elements [110, 230, 231]. For example, DWs are being investigated as information carriers for promising solid-state nonvolatile information recording devices, so-called track memory [110, 232].

Spin waves (magnons) are used in magnonics as information carriers. Domain walls have been considered until recently to be undesirable elements of spin-wave devices, since the propagation of spin waves through DWs changes the SW amplitude and phase [233]. However, it is well known that walls and interfaces are natural elements along which propagating waves can be localized. For example, the 'whispering gallery' effect [234] is associated with propagation along a curved surface of an acoustic or optical wave, which undergoes multiple total internal reflection. A characteristic standing wave is formed as a result, which is pressed against the gallery walls — the so-called whispering gallery mode. Similar modes of electromagnetic waves are used to create compact optical and microwave resonators with a high Q factor up to 10^{11} [235, 236]. Spin waves can also be localized along the surface of a ferromagnetic film due to dipole interaction (Damon–Eshbach modes [145]) in the form of long-wavelength spin waves in the magnetostatic limit. They are localized in a layer whose thickness exceeds hundreds of nanometers, while films with a much thinner thickness are being investigated for use in magnonic nanodevices [237–240].

The feasibility of using domain walls as natural SW waveguides has been shown theoretically in [114]. Such waveguides can be considered an analogue of the whispering gallery modes and the features due to the one-dimensionality of the SW propagation regime. The breaking of chiral symmetry in the presence of the Dzyaloshinskii–Moriya interaction (DMI) [241, 242] leads to a previously unknown feature of whispering gallery modes — the nonreciprocity of the propagation of spin waves along Néel domain walls.

The SW propagation in indirect (S-shaped) smooth microwaveguides has been demonstrated experimentally using as an example permalloy waveguides [243]. To suppress the scattering of spin waves in the region where the microwaveguide bends, it was necessary to apply a local magnetic field that hinders the use of indirect microwaveguides in branched magnonic circuits. In a domain wall, spin wave eigenmodes localized at its center can propagate, in contrast to spin wave eigenmodes in microwaveguides, along indirect DWs without additional scattering [114] and, moreover, in the immediate vicinity of other SW propagation channels. This is true, in particular, for the frequency range that corresponds to the modes of bulk spin waves.

In a 180-degree Néel domain wall (realized, for example, in thin permalloy films), the magnetic moments rotate in the film plane, which results in an increase in magnetic space charges with opposite signs on both sides of the DW center. The charges generate a strong magnetostatic field oriented opposite to the direction of magnetization in the DW center, as a result of which the effective magnetic field of the DW decreases locally. Such a potential well is created along the DW with a width of several dozen nanometers (or even several nanometers, depending on the parameters of the magnetic material). Since spin-wave resonances depend on the effective magnetic field, locally weakened fields can form potential wells for localized spin-wave modes.

The effects of localization and quantization in micrometer-sized waveguides have been studied theoretically and experimentally [198, 244–246]. The propagation of spin-

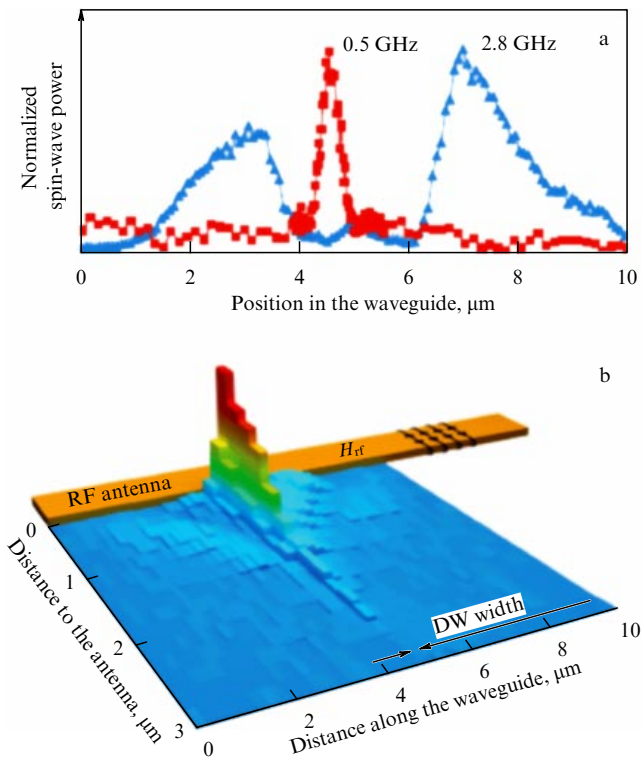

Figure 24. (a) Intensities of spin waves across the waveguide width for two excitation frequencies at a distance of 1 μm from the radio frequency (RF) antenna. The maximum intensity inside the domain wall was observed at an excitation frequency of 500 MHz (squares) and in the domains, at frequencies of about 2.8 GHz (triangles). (b) Two-dimensional distribution of the intensity of spin waves propagating along the nanowaveguide on the basis of the domain wall. Measurements were performed using MBS microscopy. Spin waves in a 40-nm-thick permalloy film are excited by a microstrip antenna [247].

wave modes strongly localized over the width of the domain wall and, importantly, in the absence of an external magnetic field, was experimentally shown in Ref. [247]. Micromagnetic simulation confirmed the experimental results, according to which spin-wave modes are strongly localized inside the domain wall in the region of relatively low frequencies (Fig. 24); with increasing frequency, the localization weakens, and to preserve the waveguide effect, it is necessary to decrease the size of the domains. We emphasize that magnetic fields were only used in [247] to change the position of the DW, i.e., to reconfigure the SW nanowaveguide.

Apart from being used as nanowaveguides, domain walls are also considered to be spin wave nanogenerators [248]. If fixed DWs are pumped by a spin-polarized current in two-layer ferroelectric–ferromagnetic structures, the predicted radiation frequencies may be as high as 100 GHz at wavelengths up to 20 nm [249]. Moreover, the coherence of spin-wave emission in parallel DWs opens up prospects for the implementation of Mach–Zehnder-type logic devices. The change in the spin wave phase when passing through the domain wall [233] can also be used to control the SW parameters. The DMI in ultrathin magnetic films with perpendicular anisotropy results in the dependence of the phase shift on the domain wall chirality [250]; therefore, a nanosized interferometer can be constructed on the basis of a DW (Fig. 25). The same principles underlie the spin-wave diode proposed in Ref. [128] (Fig. 26). Spin waves propagate

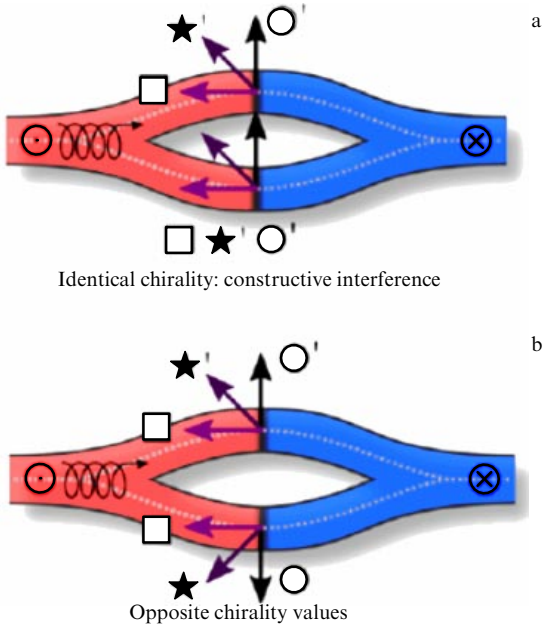

Figure 25. (Color online.) Thin-film interferometer with perpendicular anisotropy. The direction of the magnetization in the domains is indicated; spin waves propagate from left to right. Two domain walls can have the same (a) or opposite (b) chirality values. In the case of opposite chirality values, the phase shift during the passage of spin waves through the domain wall depends on the strength of the Dzyaloshinskii–Moriya interaction [250].

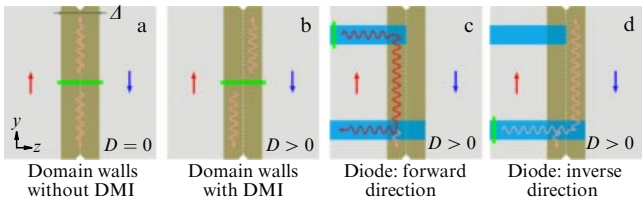

Figure 26. (Color online.) Propagation of spin waves in the domain wall (dark region) in (a) the absence ($D = 0$) and (b) the presence ($D > 0$) of DMI in the magnetic film. Red and blue arrows show the direction of magnetization in the domains. (c, d) The principle of operation of the diode for SW ($D > 0$). The input and output waveguides are marked in blue. The transfer of the magnetic moment during the passage of spin waves from the SW source (shown by the green strip) to the output channel depends on the direction of the SW propagation. The spin wave travels from top to bottom (Fig. c, forward direction for an SW diode) and is blocked when it passes from bottom to top (Fig. d, reverse direction for an SW diode) [125].

in the absence of DMI identically in both directions along the DW (Fig. 26a). In the presence of DMI (Fig. 26b–d), the propagation of the spin wave inside the waveguide channel formed by the DW is nonreciprocal. The position of the domain walls and, consequently, the transmission efficiency can be changed by magnetic field or electric current by means of STT/SOT.

Thus, DWs are considered key elements of spin-wave devices for information processing: sources of spin waves, nanoantennas, nanowaveguides, and devices for controlling SW parameters. The DW position and parameters are usually controlled using a magnetic field [110, 226–229] and, in conducting materials, also using an electric current [79, 251]. When spin waves pass through the DW, not only does the SW phase change [223, 233], but momentum can also be transferred to the DW [252, 253] and the DW begins to move under the effect of spin waves [254–256]. DWs can also move in the case of temperature gradients [257, 258] and mechanical strains [259, 260]. A highly localized effect on the DW can, in principle, be provided by laser pulses, especially if paired with plasmon elements. In connection with this, the feasibility of fully optical control of the DW position and velocity are being investigated both theoretically [261, 262] and experimentally [262–265]. The regularities of the motion of domain walls under the effect of laser pulses are most clearly manifested when the motion is initiated by a single laser pulse [241]. It has been shown that DW motion occurs in such a case in three stages, is of an inertial nature, and continues for a time that is more than an order of magnitude longer than the duration of the laser pulse; the direction of DW motion can be controlled by changing the direction of the circular polarization of the laser beam [264].

An important area in exploring the properties of DWs is the search for their possible application in high-performance devices. The nano- and microsecond duration scale of DW motion has been previously studied. This is largely due to the DW velocity of 10–100 m s^{-1} in most of the materials under study, as well as to the specific features of the methods employed for detecting dynamic DWs, and to the needs of practical applications of domains and domain walls in magneto-optical devices and as information carriers in memory devices based on cylindrical magnetic domains and vertical Bloch lines [202–205, 266, 267]. It should be noted that domain walls can move at a very high speed, up to 20 km s^{-1}, in orthoferrite plates [268, 269] and at a speed of up to 3–4 km s^{-1} in ferrite–garnet films [270, 271]. DWs are accelerated in these cases almost to the spin wave speed, whose magnitude is the limiting factor. DW velocities of more than 2 km s^{-1} were observed in amorphous microwires [272]. It should be noted that at such velocities the domain wall passes several dozen nanometers in several dozen picoseconds, which can be used in high-performance spintronic nanodevices.

An urgent task is to develop methods to study the DW dynamics on the nanometer scale, since the capacities of optical polarization microscopy are limited by the diffraction limit, magnetic force microscopy is only applicable for studying static domain structures, and the exploration of DW dynamics using X-ray methods and electron microscopy [273] is limited, in particular, by the specific requirements for the specimens under study. Domain wall displacements smaller than the optical resolution limit were demonstrated using Hall micromagnetometry [274, 275]. This method is applicable to study the relatively low-frequency DW dynamics. To study the DW dynamics in magnetic films with a regular domain structure, which can be considered a phase diffraction grating [276–278], a method has been developed for real-time spatial filtering of the output optical flux using the Fourier transform of the domain structure and a pulsed transient response. This advancement allows increasing the sensitivity to the displacement of domain walls to 5 nm and their dynamics being recorded with a time resolution of 1 ns [279]. Owing to the use of femtosecond X-ray pulses of a free electron laser for dynamic probing of magnetic domain structures, DW broadening by 20 nm was recorded as a result of exposure of a Co/Pt multilayer film to femtosecond IR laser pulses [262].

Magnetic films for nanomagnonics, despite their small thickness (varying from dozens of nanometers to several

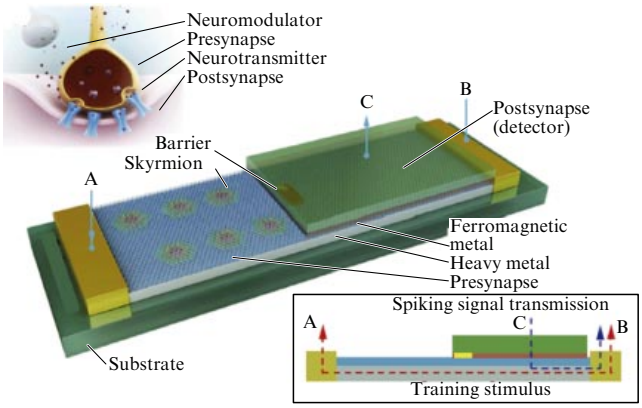

Figure 27. (Color online.) Skyrmions in the proposed design of a neuromorphic processor [286].

angstroms), are the basis for the production of various 3D magnetic spin configurations that are of interest for numerous spintronic applications [231]. Bloch lines and points are examples of such configurations in DWs. Skyrmions, spin textures with nontrivial topological charges [280–282], feature interesting properties. Skyrmions are highly resistant to external disturbances, and their size in the limiting case is only 1–2 nm. Films with skyrmions can be of subnanometer thickness; a current density of 10^3 A cm^{-2} is in some cases sufficient to move skyrmions. Skyrmions are usually observed in chiral magnetic systems, but they can also form in films with perpendicular anisotropy based on conventional ferromagnetic metals, where the DMI is absent, using local modification of the magnetic film parameters [283]. Skyrmions maintain stability in this case at room temperature and in the absence of an external magnetic field.

Skyrmions are topologically equivalent to the so-called soft cylindrical magnetic domains that do not contain Bloch lines in the DW. Similar to the usage several decades ago of cylindrical magnetic domains [202], skyrmions are now used as a basis for the development of logic devices for neuromorphic logic [284, 285], including neuromorphic computers (Fig. 27). A characteristic feature of skyrmions that affects their application in spintronic and magnonics devices is their interaction with spin waves, which manifests itself, for example, in the motion of skyrmions under the SW effect [30, 44].

7. Magnonic oscillators and detectors

The excitation of oscillations in nanoscale magnonic structures due to the spin-momentum transfer effect has attracted great interest in recent years in connection with the prospects for creating miniature and widely tunable microwave oscillators and detectors [287, 288]. Two basic designs of oscillators have been proposed (see review [288]): so-called spin-transfer nano-oscillators (STNOs) and spin Hall nano-oscillators (SHNOs), based on the transfer of spin moment in the first case from a ferromagnetic material with a fixed magnetization, and in the second, on the transfer of the spin moment due to the spin Hall effect from a heavy metal layer with a strong spin-orbit interaction. The basic designs of such oscillators are shown in Fig. 28. Due to the effect of spin moment transfer in ferromagnetic layers, compensation for losses in the system and precession of magnetization in the microwave range can occur.

The main disadvantages of such oscillators are the low output power of the generated oscillations (from less than 1 pW to hundreds of microwatts) and a large spectral line width (several dozen megahertz at a frequency of several gigahertz). A natural solution to improve these characteristics is to synchronize a multitude of the oscillators. The synchronization of STNO and SHNO by a common current [120, 289–293], spin waves [294, 295], and magnetic dipole interaction [119, 296–298] has been previously studied. Currently, the best experimental results are attained if 9 [120] and 64 [293] SHNOs are synchronized by a common current. The output power from such oscillators is detected due to the effects of giant or tunneling magnetoresistance for STNO and Hall spin resistance for SHNOs [288].

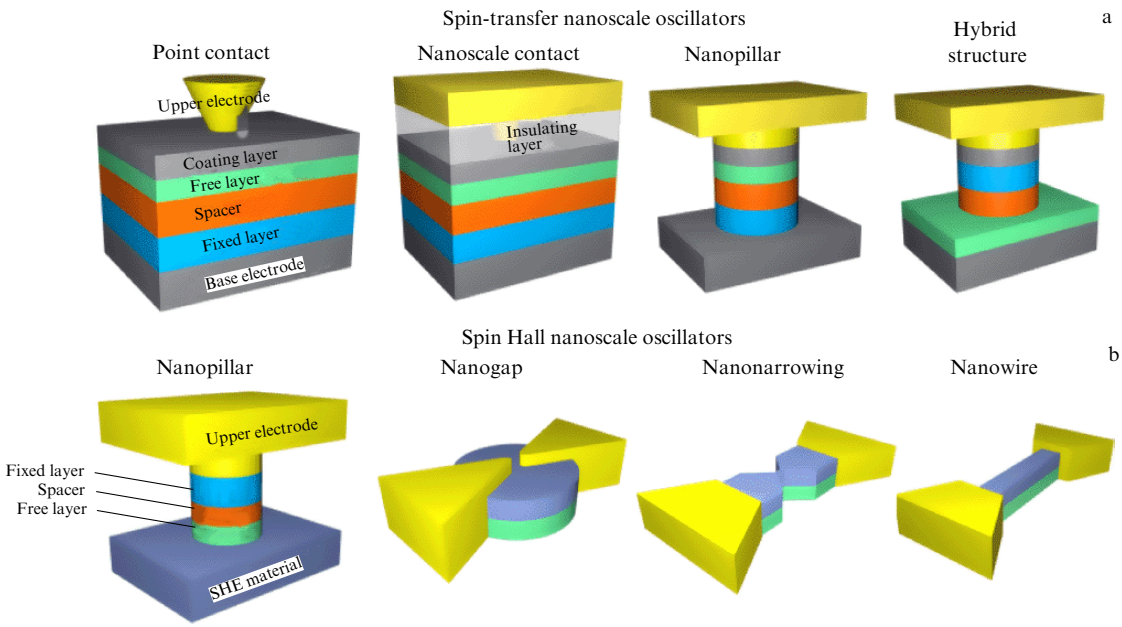

Figure 28. (Color online.) Basic designs of spin-transfer nano-oscillators (a) and spin Hall nano-oscillators (b).

The operation of magnon oscillators is most often described in theoretical terms using the Hamiltonian formalism [299], according to which the initial LLG equation with an additional term is transformed into equations for complex spin-wave amplitudes in the working ferromagnetic layer. It should be noted that the resulting equations for spin-wave amplitudes coincide with the truncated equations for macroscopic van der Pol oscillators that take into account regeneration, damping, and nonisochronism (the dependence of the oscillation frequency on the amplitude).

Generation of magnons in YIG/Pt structures has been actively studied recently in connection with the advancement in the technology for producing YIG ultrafilms several dozen nanometers thick [78, 300, 301]. Figure 29 shows in particular the design of a magnonic oscillator based on a YIG/Pt two-layer structure located in an external magnetic field H_0. MBS was used to show experimentally in [301] that, when an electric current flows through a Pt layer, an uncompensated spin moment emerges in the YIG, which leads to the generation of magnons.

The detection of microwave oscillations using magnon oscillators due to the spin-diode effect can be considered a phenomenon opposite to generation [302]. If an alternating current flows through an oscillator or an alternating electromagnetic field is applied, a constant voltage is generated at the oscillator output. Therefore, the oscillator can be used to detect alternating microwave signals. In the first experiments, the efficiency of rectifying an alternating signal did not exceed 1.4 mV mW^{-1} [302]. Later, study [303] attained a sensitivity of 12,000 mV mW^{-1} at room temperature when a bias current was passed through the specimen. It should be noted that the limiting sensitivity of commercially available Schottky diodes does not exceed 4,000 mV mW^{-1}. Active research is currently underway in the field of vortex spin diodes, the limiting sensitivity of which can be as high as 40,000 mV mW^{-1} [304].

Mutually synchronized ensembles of magnonic oscillators and spin detectors can be used to construct synthesizers of a discrete frequency grid in the microwave range [305, 306], spectrum analyzers [307, 308], broadband communication devices [309], and hardware-implemented neuromorphic networks [310].

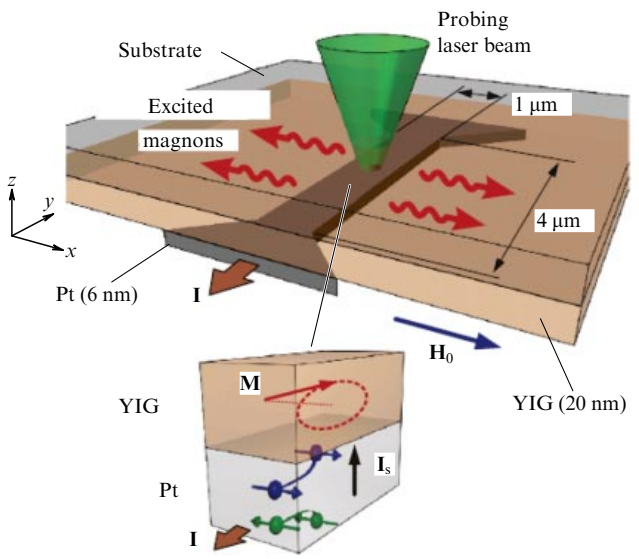

Figure 29. Design of a magnon oscillator based on the YIG/Pt structure [301]. I and I_s are electric and spin current, respectively.

8. Terahertz magnonics

The frequencies of the oscillations arising in magnon generators are proportional to the effective magnetic field, which includes the external field, the anisotropy field, and the magnetostatic field; these frequencies may be as high as dozens of gigahertz. However, the requirements for increasing the operating frequencies of magnetoelectronic and spintronic elements and devices have stimulated wide-scale fundamental research into ferro- and antiferromagnetic (AFM) spintronics and magnonics. Spin waves in magnetic materials can exist in a wide frequency range, from several megahertz to several hundred terahertz [311–313]. The frequency of spin waves (magnons) and, consequently, their velocity strongly affect the characteristics of magnonic devices. The use of terahertz frequencies in magnonic devices for generating and detecting signals and operating ultrafast information processing devices requires the development of a technology for the production of appropriate materials and methods for efficient excitation of magnons in the terahertz range. Research is focused on the development of low-energy tools for excitation, manipulation, and detection of magnons at the nanometer scale, which in turn can stimulate the development of computational applications.

The spectra of spin waves (magnons) usually consist of several branches, acoustic and optical, and the dispersion properties of high-frequency magnons are controlled by changes in the exchange magnetic interaction [314]. An alteration of the exchange parameters within a layer and between layers in structures may seem at first glance a simple task, since these quantities depend on the distances between magnetic atoms. However, it has been shown that it is rather difficult to change the interlayer exchange parameters in ferromagnetic metals when altering interatomic distances. Experiments on two-layer thin films of iron and tungsten with and without a gold buffer layer have shown that adding an Au layer leads to a significant decrease in the magnon energy. In addition to determining the nature of the exchange interaction, of importance is the issue of damping of THz magnons. The main mechanism of damping of THz magnons in ferromagnets is their decay into excitations of an electron–hole pair (so-called Stoner excitations). If such excitations exist in the region where magnons are excited, they can cause significant damping. There are usually other mechanisms of damping in magnetic bodies, for example, phonon and impurity scattering, multi-magnon scattering, and spin-orbit damping [2].

When an ordered spin system with a given dimensionality undergoes a second-order phase transition, the dependence of the magnetization on temperature can be described in terms of thermal excitations of magnons. However, the behavior of the magnons themselves as a function of temperature and the transition temperature T_c has not yet been explored. High-resolution spin-polarized spectroscopy of electron energy loss was used to study THz magnons excited in ultrathin ferromagnetic materials as a function of temperature. The energy and lifetime of magnons were shown in [2] to decrease with increasing temperature. Temperature-induced normalization of the energy and lifetime of magnons depends on the wave vector. Multi-magnon scattering becomes the main damping mechanism at high temperatures, while the Landau damping barely changes with temperature and turns out to be the main mechanism at low temperatures. The investigation of physical quantities that determine the propagation distance of mag-

nons, such as energy losses and lifetime, has shown that THz magnons maintain their propagation character even at temperatures that significantly exceed T_c for wavenumbers up to $\mathring{A}^{-1}$.

Currently, experimental and theoretical studies provide a description of a number of materials in which the frequencies of magnetic oscillations can reach several THz. The exchange interaction in FePd is sufficiently strong for the existence of magnons with a frequency of 7 THz [311]. Excitations in such a system can propagate over several dozen nanometers in a time of the order of 1 ps. The presence of the Dzyaloshinskii–Moriya exchange interaction also sets the nonreciprocity of propagation [315] of magnons when an external field is applied in the plane of the film. Experimental study [316] describes a method to excite terahertz oscillations in layered structures of ferromagnetic and nonmagnetic films, for example, Pt/Co, Gd/Co, 3–10 nm thick. An external source of oscillations is a 120-fs pulse from a femtosecond laser with an 800-nm wavelength. The unbalanced system of spins performs as a source of electromagnetic THz radiation and spin current in the films until it comes to equilibrium. The duration of such transient processes is several picoseconds, which is much longer than the pulse duration. At the ferromagnetic material–heavy metal interface, the spin current in the FM film is converted into a charge current as a result of the inverse spin Hall effect. The current density and THz-radiation power do not depend in such structures on the laser pulse polarization.

To control magnons in the THz range, it is possible to create, in addition to single FM layers, quasiperiodic structures that consist, for example, of cobalt and permalloy layers. Magnonic bandgaps in the THz frequency range were studied in [313] in periodic and quasiperiodic (the sequence of superposition of layers is determined by the Fibonacci sequence) magnonic crystals. The theoretical model is based on the Heisenberg magnetic Hamiltonian in the exchange mode and the transfer matrix method in the random phase approximation. The structure of bulk bands is similar for periodic setups to those found in photonic crystals, while for quasi-periodic multilayer structures, it has additional transmission bands similar to those found in doped electronic materials. Since the structure of the bandgaps depends on the nature of the periodicity of the human-made magnonic crystal, the number of bandgaps is larger for a quasiperiodic MC, and they have a smaller width than those in a periodic MC. However, these bandgaps lie in the THz frequency range due to the exchange interaction; thus, the dedicated structuring of the layers makes it possible to control the transmission bands for spin waves.

Another widely represented class of materials for employment in THz magnonics is antiferromagnets, which are of greatest interest as candidates for using the THz frequency range of magnetic excitations. The internal arrangement of spins in the atomic lattice of antiferromagnets has a complex structure that consists of two coupled spin sublattices; for compensated AFMs, the total magnetization is zero. Nevertheless, strong exchange interactions between the spin sublattices provide resonance frequencies in the THz range, high compared to those in conventional ferromagnets. Such studies have intensified over the past few years in many research centers; the results of the studies have been published, notably, in original papers and reviews [2, 3, 312, 317–320]. The prospects for using AFM are associated with the feasibility of creating devices for the generation, reception, and processing of signals that operate at terahertz frequencies, in particular, using AFM materials without the application of an external magnetic bias field [317]. This is achieved due to the strong exchange field in the AFM [321–323]. Designs of AFM-based terahertz oscillators [324], rectifiers [325], and spin current converters [326] have been proposed. Paper [327] presents the results of experiments on the excitation of THz spin waves in an AFM with weak ferromagnetism (hematite α-Fe_2O_3) due to the spin Hall effect and their detection using the inverse spin Hall effect.

Terahertz spintronics and magnonics seem to be promising areas, in particular, for creating a component base for non-CMOS electronics (CMOS — complementary metal–oxide–semiconductor technology) [317]. The use of terahertz spintronic transistors is optimal from the point of view of reducing energy losses, since they enable the Joule losses that occur in conventional electronics to be removed (or significantly suppressed).

It is also of importance to develop terahertz wave emitters, since the emission band controlled by the exchange energy is 1–20 THz, a value which is much larger than that of existing terahertz radiation generators based on GaAs heterostructures (1–3 THz). AFM spintronic generators of terahertz radiation will be used in medical and biological spectrometry.

A theoretical model is presented in [324] that describes oscillators with frequencies in the THz range in structures that contain a biaxial antiferromagnet (NiO) and heavy metal (Pt). A direct electric current passing through the Pt layer, due to the spin Hall effect, creates a perpendicularly polarized spin current that flows into the AFM layer. The spin current, in turn, creates a nonconservative torque (STT) for the magnetization of the sublattices. If the spin current is polarized perpendicular to the AFM ground state (along the hard axis of the AFM), it deflects the magnetization vectors from their equilibrium orientation in the opposite direction. Due to this, a strong effective field emerges, which leads to uniform rotation (in the absence of anisotropy in the plane) of the sublattice magnetizations in the plane perpendicular to the spin current polarization.

Thus, a direct current with a density of the order of $10^8 - 10^9$ A cm^{-2} enables auto-oscillation frequencies of 0.1–2.0 THz to be attained. It has also been shown that the current density can be reduced to a value several times lower than the threshold magnitude, which is only necessary for the excitation of oscillations.

Magnon excitations in AFM NiO nanowires were studied in [328]. Spin waves in the THz range were excited by a polarized laser pulse due to the magneto-optical Faraday effect in two-magnon scattering processes. The magnetization vectors of such waveguides, whose height is 700 nm and average width is 100 nm, are directed along the nanowire. Standing bulk and surface spin waves were detected using Raman spectroscopy. The square shape of the waveguide section is ensured by the conditions for the growth of such structures; therefore, these structures are waveguides with fairly smooth boundaries without defects. The oscillation frequency for bulk spin waves is as high as 43 THz, and for surface waves, of the order of 9–10 THz. The standing wave type is determined by the direction of the external constant magnetic field. For example, if a field is applied along the magnetization, standing waves of both types are excited, while if applied in the perpendicular direction, only surface waves are excited.

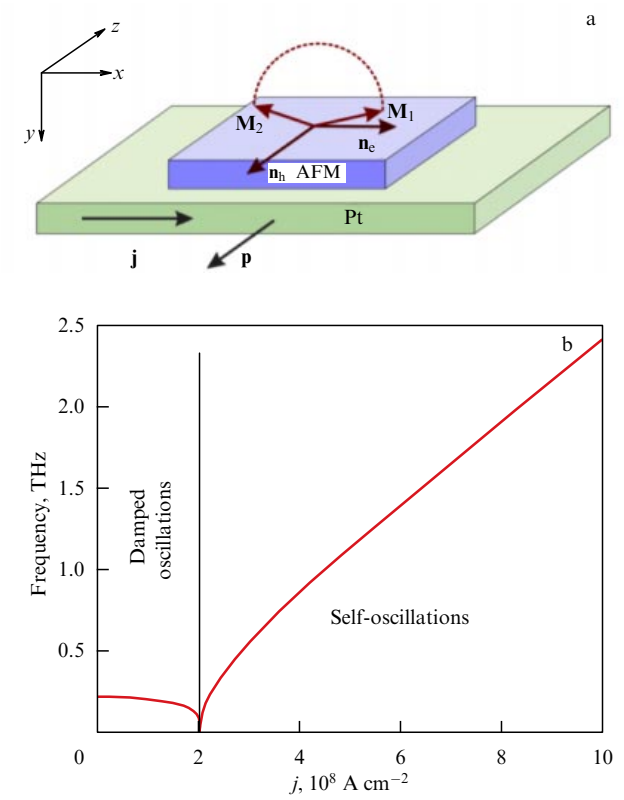

Figure 30. (a) Design of an emitter of THz oscillations based on the AFM/Pt junction; $\mathbf{n}_e$ and $\mathbf{n}_h$ are vectors of easy and hard axes of anisotropy, $\mathbf{p}$ is the spin current polarization vector. (b) Oscillation frequency as a function of the density of the current flowing through the specimen.

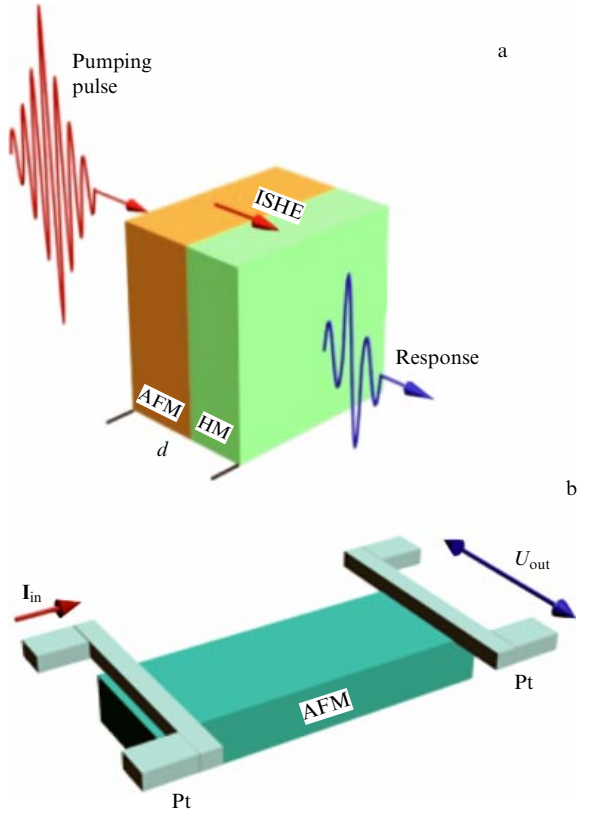

Figure 31. (a) Emitter of electromagnetic THz waves with external excitation (HM is a heavy metal) and (b) a waveguide of spin THz waves based on the AFM/Pt junctions. I_{in} is the input electric current and U_{out} is the output voltage.

Another prototype of a THz-wave generator consists of a heavy metal layer with a large spin-orbital interaction (for example, platinum) and an AFM layer with easy-plane anisotropy, in which the nonzero magnetization $\mathbf{m}_{DMI}$ is due to the DMI forces [329]. If a direct electric current flows in the metal layer, a spin current emerges due to the spin Hall effect [91] that flows perpendicular to the interface between the metal and the AFM layer (Fig. 30a).

In entering the AFM layer, this spin current deviates the magnetization $\mathbf{m}_{DMI}$ from the equilibrium value, which is due to the strong exchange interaction in the AFM. Owing to the exchange interaction between the magnetization AFM sublattices, these sublattices and the vector $\mathbf{m}_{DMI}$ begin to oscillate around the hard axis of the AFM. As a result, due to the inverse spin Hall effect, dipole radiation emerges, which can be detected in the neighboring dielectric layer adjacent to the AFM layer. The radiation frequency is proportional to the exchange interaction energy that corresponds to the THz frequency range. The radiation power is proportional to the current flowing in the metal layer and the radiation frequency and may be of the order of several microwatts. The dependence of the oscillation frequency on the transmitted current displayed in Fig. 30b consists of two segments: a descending branch, where the oscillator operates in a damped oscillation mode, and an ascending one, where the oscillator operates in a self-oscillating mode.

AFM spintronics with optical pulsed excitation of magnetic dynamics is actively developing. Femtosecond laser pulses were used in pioneering experiments [330] to generate terahertz pulses during reversal of FM material magnetization as a result of the emergence of a high-frequency current due to the inverse spin Hall effect. Terahertz emitters based on heterostructures with AFM layers with tilted magnetic sublattices (for example, based on hematite α-Fe_2O_3) seem to be promising (Fig. 31a) [331]. In particular, a model of an AFM waveguide for terahertz spin waves has been proposed (Fig. 31b) [332], which can be used to create terahertz waveguides and spin wave resonators based on AFM heterostructures intended, for example, for application in neuromorphic calculations [6].

9. Conclusion. Prospects for applications and unsolved problems

Prospects for the practical use of ferrite–semiconductor structures in information processing and storage systems are directly related to the feasibility of integrating passive film ferrite and active semiconductor components of monolithic integrated circuits within a unified production process [333]. The technologies of magnetron sputtering and pulsed laser deposition currently being used enable obtainment of ferrite layers up to several hundred nanometers thick on semiconductor substrates of various types (Si, GaAs) [171, 334–336]. Further improvement in these technologies is aimed at obtaining films with uniform magnetic properties with controllable parameters and the minimum possible width of ferromagnetic resonance lines.

It is also worth noting that superconductor/ferromagnetic heterostructures may be used to create spin-wave devices tunable due to magnon–fluxon interaction, in which reconfi-

gurable magnon–crystal structures are formed as a result of local excitation of Abrikosov vortices [337, 338].

Quantum fluctuations in magnonic nanostructures are also actively being explored [339–342]. The presence of quantum fluctuations during the flow of a spin-polarized current through multilayer magnetic nanostructures at low temperatures (several kelvin) results in the excitation of magnons in a wide frequency range (from several gigahertzes to hundreds of gigahertz), which can be used as a source of oscillations in THz magnonics [339].

Interesting prospects open up if domain walls are used in magnonics devices as the basis for many reconfigurable elements: spin wave sources, nanowaveguides, interferometers, spin wave diodes, and other devices for controlling spin wave parameters [247–250, 343], and if spin waves are employed for control of domain walls and skyrmions in logic and memory devices of nanospintronics [30, 44, 254–256]. The feasibility of creating ultrafast devices based on domain walls using laser pulses for completely optical control of local parameters and the position of domain walls are under intense study [261–265].

Active research is currently underway in the use of graphene in spintronics [344] and magnonics [345]. The transport of spin-polarized electrons [346, 347] and the spin Hall effect in graphene [77] have been studied. The spin–orbit interaction in graphene is weak, in contrast to that in heavy metals, and the effect is associated with a zero bandgap and Zeeman splitting of levels in a magnetic field, the latter being two orders of magnitude higher than in semiconductors [348]. We also note the feasibility of using graphene to detect variable signals in multilayer structures, for example, graphene/YIG [345].

Thus, we presented in this review a systematic description of recent studies in dielectric magnonics and magnonic spintronics. Considered in detail are analytical and numerical methods used to describe physical processes in magnonic micro- and nanostructures, spin effects that underlie magnonic spintronics, and experimental methods applied to study magnonic structures.

The results presented in this review were obtained with the support of a grant from the Government of the Russian Federation for state support of academic research conducted under the guidance of leading scientists in tertiary educational institutions, research institutions, and national research centers of the Russian Federation (project no. 075-15-2019-1874), the Government of the Russian Federation (agreement 074-02-2018-286), the Russian Science Foundation (grant 19-19-00607), the Russian Foundation for Basic Research (grants 18-29-27018, 18-29-27020, 18-29-27026, 18-37-20005, 18-37-20048, 18-57-16001, 19-29-03015, 18-57-76001, 18-07-00509, 18-52-16006), and grants from the President of the Russian Federation for young candidates of sciences, nos MK-283.2019.8, MK-3607.2019.9, and MK-3650.2018.9.

References

1. Nikitov S A et al. *Phys. Usp.* **58** 1002 (2015); *Usp. Fiz. Nauk* **185** 1099 (2015)
2. Jungwirth T et al. *Nat. Nanotechnol.* **11** 231 (2016)
3. Baltz V et al. *Rev. Mod. Phys.* **90** 015005 (2018)
4. Bukharaev A A et al. *Phys. Usp.* **61** 1175 (2018); *Usp. Fiz. Nauk* **188** 1288 (2018)
5. Sadovnikov A V et al. *Phys. Rev. Lett.* **120** 257203 (2018)
6. Torrejon J et al. *Nature* **547** 428 (2017)
7. Brächer T, Pirro P *J. Appl. Phys.* **124** 152119 (2018)
8. Chumak A V, Serga A A, Hillebrands B *J. Phys. D* **50** 244001 (2017)
9. Gurevich A G, Melkov G A *Magnetization Oscillations and Waves* (Boca Raton, FL: CRC Press, 1996)
10. Yablonovitch E *Phys. Rev. Lett.* **58** 2059 (1987)
11. John S *Phys. Rev. Lett.* **58** 2486 (1987)
12. Joannopoulos J D et al. *Photonic Crystals: Molding the Flow of Light* 2nd ed. (Princeton, NJ: Princeton Univ. Press, 2011)
13. Krawczyk M, Puszkarski H *Phys. Rev. B* **77** 054437 (2008)
14. Krawczyk M et al. *J. Appl. Phys.* **108** 093909 (2010)
15. Neusser S et al. *Phys. Rev. B* **84** 094454 (2011)
16. Romero Vivas J et al. *Phys. Rev. B* **86** 144417 (2012)
17. Kumar N, Prabhakar A *IEEE Trans. Magn.* **49** 1024 (2013)
18. Kumar D et al. *J. Appl. Phys.* **115** 043917 (2014)
19. Zivieri R *IEEE Trans. Magn.* **50** 1100304 (2014)
20. Lisenkov I et al. *J. Magn. Magn. Mater.* **378** 313 (2015)
21. Rychly J, Klos J W *J. Phys. D* **50** 164004 (2017)
22. Damon R W, Eshbach J R *J. Appl. Phys.* **31** S104 (1960)
23. Kittel C *Introduction to Solid State Physics* 7th ed. (New York: Wiley, 1996)
24. Parekh J, Tuan H *IEEE Trans. Magn.* **13** 1246 (1977)
25. Graczyk P, Krawczyk M *Phys. Rev. B* **96** 024407 (2017)
26. Snyder A W, Love J D *Optical Waveguide Theory* (London: Chapman and Hall, 1983)
27. Klos J W, Zozoulenko I V *Phys. Rev. B* **82** 081414(R) (2010)
28. Nakata K et al. *Phys. Rev. B* **96** 224414 (2017)
29. Ahmed M H, Jeske J, Greentree A D *Sci. Rep.* **7** 41472 (2017)
30. Shen K *New J. Phys.* **20** 043025 (2018)
31. Mousavi Z, Rabani H, Mardaani M *J. Magn. Magn. Mater.* **484** 367 (2019)
32. Ashcroft N W, Mermin N D *Solid State Physics* (New York: Holt, Rinehart and Winston, 1976)
33. Nicorovici N A, McPhedran R C, Botten L C *Phys. Rev. E* **52** 1135 (1995)
34. Botten L C et al. *Prog. Electromagn. Res.* **41** 21 (2003)
35. Es'kin V A et al. *Phys. Rev. E* **86** 067601 (2012)
36. Asatryan A A et al. *Phys. Rev. B* **88** 035127 (2013)
37. Drozdovskii A V, Nikitin A A, Ustinov A B *J. Phys. Conf. Ser.* **661** 012063 (2015)
38. Urmancheev R, Kalyabin D, Nikitov S *J. Magn. Magn. Mater.* **401** 50 (2016)
39. Dadoenkova Yu S et al. *IEEE Trans. Magn.* **53** 2501005 (2017)
40. Blundell S J *J. Phys. Condens. Matter* **6** 10283 (1994)
41. Nikitov S A, Tailhades Ph, Tsai C S *J. Magn. Magn. Mater.* **236** 320 (2001)
42. Kittel C *Introduction to Solid State Physics* 8th ed. (Hoboken, NJ: Wiley, 2005)
43. Thompson F et al. *J. Phys. A* **51** 495204 (2018)
44. Li R *Phys. Rev. B* **97** 085430 (2018)
45. Lisenkov I, Kalyabin D, Nikitov S *Appl. Phys. Lett.* **103** 202402 (2013)
46. Barabanenkov Yu et al. *Phys. Rev. B* **91** 214419 (2015)
47. Lage E J S, Stinchcombe R B *J. Phys. C* **10** 295 (1977)
48. Urbaniak-Kucharczyk A *Phys. Status Solidi B* **189** 239 (1995)
49. Rowlands D A, Staunton J B, Györffy B L *Phys. Rev. B* **67** 115109 (2003)
50. Sheng P *Introduction to Wave Scattering, Localization and Mesoscopic Phenomena* (Berlin: Springer, 2006)
51. Avgin I, Boukahil A, Huber D L *Physica E* **42** 2331 (2010)
52. Jin J et al. *Phys. Rev. B* **80** 115101 (2009)
53. Mitsumata C, Tomita S *Phys. Rev. B* **84** 174421 (2011)
54. Kruglyak V V et al., in *Metamaterial* (Ed. X-Y Jiang) (London: InTech, 2012) p. 341
55. Zivieri R, Giovannini L *Metamaterials* **6** e127 (2012)
56. Schrefl T et al. "Numerical methods in micromagnetics (finite element method)", in *Handbook of Magnetism and Advanced Magnetic Materials* (Eds H Kronmüller et al.) (New York: John Wiley and Sons, 2007)
57. Mruczkiewicz M et al. *Phys. Rev. B* **96** 104411 (2017)
58. Shaimanov A N, Khabarov K M, Baryshev A V *J. Magn. Magn. Mater.* **485** 54 (2019)
59. Beginin E N et al. *Appl. Phys. Lett.* **112** 122404 (2018)
60. Popov P A et al. *J. Magn. Magn. Mater.* **476** 423 (2019)

61. Fischbacher T et al. *IEEE Trans. Magn.* **43** 2896 (2007)
62. Kakay A, Westphal E, Hertel R *IEEE Trans. Magn.* **46** 2303 (2010)
63. Scholz W et al. *Comput. Mater. Sci.* **28** 366 (2003)
64. Chang R et al. *J. Appl. Phys.* **109** 07D358 (2011)
65. Schöberl J *Comput. Visual. Sci.* **1** 41 (1997)
66. Chi K H, Zhu Y, Tsai C S *IEEE Trans. Magn.* **49** 1000 (2013)
67. Hao Y, Mittra R *FDTD Modeling of Metamaterials: Theory and Applications* (Norwood, MA: Artech House, 2009)
68. Donahue M J "OOMMF user's guide, version 1.0", Technical Report 6376 (Gaithersburg, MD: NIST, 1999) https://doi.org/10.6028/NIST.IR.6376
69. Kim S-K, Lee K-S, Han D-S *Appl. Phys. Lett.* **95** 082507 (2009)
70. Vivek T, Sabareesan P *IEEE Trans. Magn.* **55** 7200106 (2019)
71. Vansteenkiste A et al. *AIP Adv.* **4** 107133 (2014)
72. Lopez-Diaz L et al. *J. Phys. D* **45** 323001 (2012)
73. NVIDIA CUDA C Programming Guide (2014)
74. Popov P A et al. *J. Commun. Technol. Electron.* **63** 1431 (2018); *Radiotekh. Elektron.* **63** 1285 (2018)
75. Ralph D C, Stiles M D *J. Magn. Magn. Mater.* **320** 1190 (2008)
76. Hellman F et al. *Rev. Mod. Phys.* **89** 025006 (2017)
77. Sinova J et al. *Rev. Mod. Phys.* **87** 1213 (2015)
78. Demidov V E et al. *Phys. Rep.* **673** 1 (2017)
79. Slonczewski J C *J. Magn. Magn. Mater.* **159** L1 (1996)
80. Berger L *Phys. Rev. B* **54** 9353 (1996)
81. Tsoi M et al. *Phys. Rev. Lett.* **80** 4281 (1998)
82. Myers E B *Science* **285** 867 (1999)
83. Sun J Z *J. Magn. Magn. Mater.* **202** 157 (1999)
84. Katine J A et al. *Phys. Rev. Lett.* **84** 3149 (2000)
85. Gulyaev Yu V et al. *Phys. Usp.* **52** 335 (2009); *Usp. Fiz. Nauk* **179** 359 (2009)
86. Zhang S, Levy P M, Fert A *Phys. Rev. Lett.* **88** 236601 (2002)
87. Zhang S, Li Z *Phys. Rev. Lett.* **93** 127204 (2004)
88. Stiles M D, Xiao J, Zangwill A *Phys. Rev. B* **69** 054408 (2004)
89. Urazhdin S *Phys. Rev. B* **69** 134430 (2004)
90. Zvezdin A K, Zvezdin K A, Khval'kovskii A V *Phys. Usp.* **51** 412 (2008); *Usp. Fiz. Nauk* **178** 436 (2008)
91. D'yakonov M I, Perel' V I *JETP Lett.* **13** 467 (1971); *Pis'ma Zh. Eksp. Teor. Fiz.* **13** 657 (1971)
92. Hirsch J E *Phys. Rev. Lett.* **83** 1834 (1999)
93. Kato Y K *Science* **306** 1910 (2004)
94. Ando K et al. *Phys. Rev. Lett.* **101** 036601 (2008)
95. Liu L et al. *Phys. Rev. Lett.* **106** 036601 (2011)
96. Liu L et al. *Phys. Rev. Lett.* **109** 096602 (2012)
97. Garello K et al. *Nat. Nanotechnol.* **8** 587 (2013)
98. Kim J et al. *Nat. Mater.* **12** 240 (2013)
99. Wang H L et al. *Phys. Rev. Lett.* **112** 197201 (2014)
100. Tserkovnyak Y, Brataas A, Bauer G E W *Phys. Rev. Lett.* **88** 117601 (2002)
101. Azevedo A et al. *J. Appl. Phys.* **97** 10C715 (2005)
102. Tserkovnyak Ya et al. *Rev. Mod. Phys.* **77** 1375 (2005)
103. Saitoh E et al. *Appl. Phys. Lett.* **88** 182509 (2006)
104. Mosendz O et al. *Phys. Rev. Lett.* **104** 046601 (2010)
105. Ando K et al. *J. Appl. Phys.* **109** 103913 (2011)
106. Uchida K et al. *Nature* **455** 778 (2008)
107. Gravier L et al. *J. Appl. Phys.* **97** 10C501 (2005)
108. Safranski C et al. *Nat. Commun.* **8** 117 (2017)
109. Kirihara A et al. *Nat. Mater.* **11** 686 (2012)
110. Sander D et al. *J. Phys. D* **50** 363001 (2017)
111. Roldán-Molina A, Nunez A S, Fernández-Rossier J *New J. Phys.* **18** 045015 (2016)
112. Smejkal L et al. *Nat. Phys.* **14** 242 (2018)
113. Nikitin A A et al. *Appl. Phys. Lett.* **106** 102405 (2015)
114. Garcia-Sanchez F et al. *Phys. Rev. Lett.* **114** 247206 (2015)
115. Chisnell R et al. *Phys. Rev. Lett.* **115** 147201 (2015)
116. Wang X S, Zhang H W, Wang X R *Phys. Rev. Appl.* **9** 024029 (2018)
117. Wang X S, Su Y, Wang X R *Phys. Rev. B* **95** 014435 (2017)
118. Li Y-M, Xiao J, Chang R *Nano Lett.* **18** 3032 (2018)
119. Locatelli N et al. *Sci. Rep.* **5** 17039 (2015)
120. Awad A A et al. *Nat. Phys.* **13** 292 (2016)
121. Barabanenkov Yu et al. *Phys. Rev. B* **94** 184409 (2016)
122. Shutyi A M, Sementsov D I *JETP Lett.* **106** 358 (2017); *Pis'ma Zh. Eksp. Teor. Fiz.* **106** 334 (2017)
123. Galkina E G, Ivanov B A *JETP Lett.* **104** 32 (2016); *Pis'ma Zh. Eksp. Teor. Fiz.* **104** 26 (2016)
124. Wang Q et al. *Sci. Adv.* **4** e1701517 (2018)
125. Lan J et al. *Phys. Rev. X* **5** 041049 (2015)
126. Gladii O et al. *Phys. Rev. B* **93** 054430 (2016)
127. Zhang V L et al. *Appl. Phys. Lett.* **107** 022402 (2015)
128. Kim J-V, Stamps R L, Camley R E *Phys. Rev. Lett.* **117** 197204 (2016)
129. Osokin S A et al. *J. Magn. Magn. Mater.* **465** 519 (2018)
130. Lisenkov I et al. *Phys. Rev. B* **93** 214441 (2016)
131. Sadovnikov A V et al. *IEEE Magn. Lett.* **9** 3707105 (2018)
132. Sadovnikov A V et al. *JETP Lett.* **107** 25 (2018); *Pis'ma Zh. Eksp. Teor. Fiz.* **107** 29 (2018)
133. Odintsov S A, Sadovnikov A V *Izv. Vyssh. Uchebn. Zaved. Priklad. Nelin. Din.* **26** (6) 59 (2018)
134. Sadovnikov A V et al. *Phys. Rev. B* **96** 144428 (2017)
135. Sadovnikov A V et al. *IEEE Trans. Magn.* **53** (11) 1 (2017)
136. Davies C S et al. *Phys. Rev. B* **92** 020408(R) (2015)
137. Chumak A V et al. *Nat. Phys.* **11** 453 (2015)
138. Sadovnikov A V et al. *Appl. Phys. Lett.* **107** 202405 (2015)
139. Sadovnikov A V et al. *IEEE Magn. Lett.* **8** 3109904 (2017)
140. Sadovnikov A V et al. *Phys. Rev. Appl.* **7** 014013 (2017)
141. Sadovnikov A V et al. *Appl. Phys. Lett.* **109** 042407 (2016)
142. Demokritov S O (Ed.) *Spin Wave Confinement* (Singapore: Pan Stanford Publ., 2017)
143. Akhiezer A I, Bar'yakhtar V G, Peletminskii S V *Spin Waves* (Amsterdam: North-Holland, 1968); Translated from Russian: Bar'yakhtar V G, Peletminskii S V, Akhiezer A I *Spinovye Volny* (Moscow: Nauka, 1967)
144. Boardman A D, Nikitov S A, Waby N A *Phys. Rev. B* **48** 13602 (1993)
145. Damon R W, Eshbach J R *J. Phys. Chem. Solids* **19** 308 (1961)
146. Landau L D, Lifshitz E M *Phys. Z. Sowjetunion* **8** 153 (1935)
147. Zavislyak I V, Tychinskii A V *Fizicheskie Osnovy Funktsional'noi Mikroelektroniki* (Physical Basics of Functional Microelectronics) (Kiev: UMKVO, 1989)
148. Gilbert T L *IEEE Trans. Magn.* **40** 3443 (2004)
149. Ustinov A B, Kalinikos B A *Appl. Phys. Lett.* **93** 102504 (2008)
150. Kruglyak V V, Demokritov S O, Grundler D *J. Phys. D* **43** 260301 (2010)
151. Krawczyk M, Grundler D *J. Phys. Condens. Matter* **26** 123202 (2014)
152. Tacchi S et al. *Phys. Rev. Lett.* **109** 137202 (2012)
153. Brekhovskikh L M *Waves in Layered Media* (New York: Academic Press, 1980); Translated from Russian: *Volny v Sloistykh Sredakh* (Moscow: Nauka, 1973)
154. Beginin E N et al. *Appl. Phys. Lett.* **100** 252412 (2012)
155. Mruczkiewicz M et al. *Phys. Rev. B* **90** 174416 (2014)
156. Sheshukova S E et al. *IEEE Magn. Lett.* **5** 3700204 (2014)
157. Sadovnikov A V et al. *JETP Lett.* **105** 364 (2017); *Pis'ma Zh. Eksp. Teor. Fiz.* **105** 347 (2017)
158. Arkad'ev V K *Zh. Russ. Fiz.-Khim. Obshch. Ch. Fiz.* **45** 312 (1913)
159. Kittel C *Phys. Rev.* **73** 155 (1948)
160. Vonsovskii S V (Ed.) *Ferromagnetic Resonance: the Phenomenon of Resonant Absorption of a High-Frequency Magnetic Field in Ferromagnetic Substances* (Oxford: Pergamon Press, 1966); Translated from Russian: *Ferromagnitnyi Rezonans: Yavlenie Rezonansnogo Pogloshsheniya Vysokochastotnogo Elektromagnitnogo Polya v Ferromagnitnykh Veshchestvakh* (Moscow: Fizmatgiz, 1961)
161. Miles P A *Nature* **174** 177 (1954)
162. Celinski Z, Urquhart K B, Heinrich B *J. Magn. Magn. Mater.* **166** 6 (1997)
163. Anisimov A N et al. *Phys. Rev. Lett.* **82** 2390 (1999)
164. Fermin J R et al. *J. Appl. Phys.* **85** 7316 (1999)
165. De Wames R E, Wolfram T *J. Appl. Phys.* **41** 987 (1970)
166. Kooi C F et al. *J. Appl. Phys.* **35** 791 (1964)
167. Jalali-Roudsar A A, Denysenkov V P, Khartsev S I *J. Magn. Magn. Mater.* **288** 15 (2005)
168. Sun Y et al. *Appl. Phys. Lett.* **101** 152405 (2012)
169. Sun Y, Song Y-Y, Wu M *Appl. Phys. Lett.* **101** 082405 (2012)
170. Wigen P E, Zhang Z *Braz. J. Phys.* **22** 267 (1992)
171. Stognij A I et al. *J. Appl. Phys.* **118** 023905 (2015)
172. Artman J O, Charap S H *J. Appl. Phys.* **50** 2024 (1979)

173. Malinowski G, Boulle O, Kläui M *J. Phys. D* **44** 384005 (2011)
174. Ramesh M, Wigen P E *J. Magn. Magn. Mater.* **74** 123 (1988)
175. Ramesh M et al. *J. Appl. Phys.* **64** 5483 (1988)
176. Wegrowe J-E et al. *Phys. Rev. B* **61** 12216 (2000)
177. Maksymov I S, Kostylev M *Physica E* **69** 253 (2015)
178. Bilzer C et al. *J. Appl. Phys.* **101** 074505 (2007)
179. Kalarickal S et al. *J. Appl. Phys.* **99** 093909 (2006)
180. Adeyeye A O, Shimon G, in *Magnetism of Surfaces, Interfaces, and Nanoscale Materials* (Handbook of Surface Science, Vol. 5, Eds R E Camley, Z Celinski, R L Stamps) (Amsterdam: Elsevier, 2015) p. 1
181. Lee S et al. *J. Appl. Phys.* **120** 033905 (2016)
182. Banholzer A et al. *Nanotechnology* **22** 295713 (2011)
183. Klingler S et al. *J. Phys. D* **48** 015001 (2014)
184. Bousbahi K, Marcelli R *J. Appl. Phys.* **87** 5971 (2000)
185. Chumak A V et al. *Appl. Phys. Lett.* **94** 172511 (2009)
186. Sadovnikov A V et al. *Phys. Rev. B* **96** 060401(R) (2017)
187. Rousseau O et al. *Sci. Rep.* **5** 9873 (2015)
188. Kanazawa N et al. *Sci. Rep.* **6** 30268 (2016)
189. Lutsev L V et al. *J. Phys. D* **51** 355002 (2018)
190. Mandelstam L I *Zh. Russ. Fiz.-Khim. Obshch.* **58** 381 (1926); *Polnoe Sobranie Trudov* (Complete Works) Vol. 1 (Moscow: Izd. AN SSSR, 1948) p. 280
191. Brillouin L *Ann. Phys. Paris* **9** (17) 88 (1922)
192. Borovik-Romanov A S, Kreines N M, Zhotikov V G *Sov. Phys. Usp.* **21** 538 (1978); *Usp. Fiz. Nauk* **125** 355 (1978)
193. Camley R E, Mills D L *J. Appl. Phys.* **50** 7779 (1979)
194. Rojdestvenski I V, Cottam M G, Slavin A N *J. Appl. Phys.* **73** 7001 (1993)
195. Demokritov S O *Phys. Rep.* **348** 441 (2001)
196. Sandercock J R, Wettling W *J. Appl. Phys.* **50** 7784 (1979)
197. Neumann T et al. *Rev. Sci. Instrum.* **80** 053905 (2009)
198. Sebastian T et al. *Front. Phys.* **3** 35 (2015)
199. Madami M et al. *Solid State Phys.* **63** 79 (2012)
200. Demokritov S O, Demidov V E *IEEE Trans. Magn.* **44** 6 (2008)
201. Zhu Y (Ed.) *Modern Techniques for Characterizing Magnetic Materials* (Boston: Kluwer Acad. Publ., 2005)
202. Demokritov S O *J. Magn. Magn. Mater.* **126** 291 (1993)
203. Tacchi S et al. *IEEE Trans. Magn.* **46** 1440 (2010)
204. Qin H et al. *Nat. Commun.* **9** 5445 (2018)
205. Goto T et al. *Phys. Rev. Appl.* **11** 014033 (2019)
206. Tacchi S et al. *J. Phys. Condens. Matter* **29** 073001 (2016)
207. Langner T et al. *J. Phys. D* **51** 344002 (2018)
208. Kryshtal R G, Medved A V *J. Magn. Magn. Mater.* **426** 666 (2017)
209. Sadovnikov A V et al. *Appl. Phys. Lett.* **112** 142402 (2018)
210. Sadovnikov A V et al. *JETP Lett.* **108** 312 (2018); *Pis'ma Zh. Eksp. Teor. Fiz.* **108** 332 (2018)
211. Demidov V E et al. *Sci. Rep.* **5** 8578 (2015)
212. Sadovnikov A V et al. *Appl. Phys. Lett.* **108** 172411 (2016)
213. Odintsov S A et al. *JETP Lett.* **104** 563 (2016); *Pis'ma Zh. Eksp. Teor. Fiz.* **104** 576 (2016)
214. O'Keeffe T W, Patterson R W *J. Appl. Phys.* **49** 4886 (1978)
215. Bajpai S N *J. Appl. Phys.* **58** 910 (1985)
216. International Technology Roadmap for Semiconductors (2017), https://irds.ieee.org/
217. Zang J, Cros V, Hoffmann A (Eds) *Topology in Magnetism* (Cham: Springer Intern. Publ., 2018)
218. Boudiar T et al. *J. Magn. Magn. Mater.* **284** 77 (2004)
219. Sun X Y et al. *ACS Photon.* **2** 856 (2015)
220. Levinshtein M, Rumyantsev S, Shur M *Handbook Series on Semiconductor Parameters* (Singapore: World Scientific, 1996)
221. Sandercock J R *Opt. Commun.* **2** 73 (1970)
222. Sandercock J, Wettling W *IEEE Trans. Magn.* **14** 442 (1978)
223. Bayer C et al. *IEEE Trans. Magn.* **41** 3094 (2005)
224. Kalinikos B A, Slavin A N *J. Phys. C* **19** 7013 (1986)
225. Sadovnikov A V et al. *Phys. Rev. B* **99** 054424 (2019)
226. Malozemoff A P, Slonczewski J C *Magnetic Domain Walls in Bubble Materials* (Amsterdam: Academic Press, 1979)
227. Bar'yakhtar V G, Bogdanov A N, Yablonskii D A *Sov. Phys. Usp.* **31** 810 (1988); *Usp. Fiz. Nauk* **156** 47 (1988)
228. Vachaspati T *Kinks Domain Walls: an Introduction to Classical and Quantum Solitons* (Cambridge: Cambridge Univ. Press, 2006)
229. Hubert A, Schäfer R *Magnetic Domains: the Analysis of Magnetic Microstructures* (Berlin: Springer, 1998)
230. Hoffmann A, Bader S D *Phys. Rev. Appl.* **4** 047001 (2015)
231. Fernández-Pacheco A et al. *Nat. Commun.* **8** 15756 (2017)
232. Parkin S P, Hayashi M, Thomas L *Science* **320** 190 (2008)
233. Hertel R, Wulfhekel W, Kirschner J *Phys. Rev. Lett.* **93** 257202 (2004)
234. Lord Rayleigh *Philos. Mag. J. Sci. 6* **20** 1001 (1910)
235. Gorodetskii M L *Opticheskie Mikrorezonatory s Gigantskoi Dobrotnost'yu* (Optical Microresonators with Giant Q-Factor) (Moscow: Fizmatlit, 2011)
236. Kozlov D A, Kotlyar V V *Komp. Opt.* **39** 324 (2015)
237. Jungfleisch M B et al. *J. Appl. Phys.* **117** 17D128 (2015)
238. Lee A J et al. *Nat. Commun.* **8** 234 (2017)
239. Emori S et al. *Nano Lett.* **18** 4273 (2018)
240. Soumah L et al. *Nat. Commun.* **9** 3355 (2018)
241. Dzyaloshinskii I E *Sov. Phys. JETP* **5** 1259 (1957); *Zh. Eksp. Teor. Fiz.* **32** 1547 (1957)
242. Moriya T *Phys. Rev. Lett.* **4** 228 (1960)
243. Vogt K et al. *Appl. Phys. Lett.* **101** 042410 (2012)
244. Jorzick J et al. *Phys. Rev. Lett.* **88** 047204 (2002)
245. Demidov V E et al. *Appl. Phys. Lett.* **91** 252504 (2007)
246. Sebastian T et al. *Phys. Rev. Lett.* **110** 067201 (2013)
247. Wagner K et al. *Nat. Nanotechnol.* **11** 432 (2016)
248. Hermsdoerfer S J et al. *Appl. Phys. Lett.* **94** 223510 (2009)
249. Van de Wiele B et al. *Sci. Rep.* **6** 21330 (2016)
250. Buijnsters F J et al. *Phys. Rev. Lett.* **116** 147204 (2016)
251. Siddiqui S A et al. *Phys. Rev. Lett.* **121** 057701 (2018)
252. Zvezdin A K, Popkov A F *JETP Lett.* **39** 419 (1984); *Pis'ma Zh. Eksp. Teor. Fiz.* **39** 348 (1984)
253. Maho Y, Kim J-V, Tatara G *Phys. Rev. B* **79** 174404 (2009)
254. Mikhailov A V, Yaremchuk A *JETP Lett.* **39** 354 (1984); *Pis'ma Zh. Eksp. Teor. Fiz.* **39** 296 (1984)
255. Han D-S et al. *Appl. Phys. Lett.* **94** 112502 (2009)
256. Tveten E G, Qaiumzadeh A, Brataas A *Phys. Rev. Lett.* **112** 147204 (2014)
257. Tetienne J P et al. *Science* **344** 1366 (2014
258. Moretti S et al. *Phys. Rev. B* **95** 064419 (2017)
259. De Ranieri E et al. *Nat. Mater.* **12** 808 (2013)
260. Mathurin T et al. *Phys. Rev. B* **95** 140405 (2017)
261. Genkin G M, Tokman I D *Sov. Phys. JETP* **55** 887 (1982); *Zh. Eksp. Teor. Fiz.* **82** 1532 (1982)
262. Pfau B et al. *Nat. Commun.* **3** 1100 (2012)
263. Ogawa N et al. *Proc. Natl. Acad. Sci. USA* **112** 8977 (2015)
264. Gerasimov M V et al. *Phys. Rev. B* **94** 014434 (2016)
265. Quessab Y et al. *Phys. Rev. B* **97** 054419 (2018)
266. Bobeck A H *Bell Syst. Tech. J.* **46** 1901 (1967)
267. Konishi S *IEEE Trans. Magn.* **19** 1838 (1983)
268. Konishi S, Miyama T, Ikeda K *Appl. Phys. Lett.* **27** 258 (1975)
269. Bar'yakhtar V G, Ivanov B A, Chetkin M V *Sov. Phys. Usp.* **28** 563 (1985); *Usp. Fiz. Nauk* **146** 417 (1985)
270. Logunov M V, Randoshkin V V, Chervonenkis A Ya *Sov. Tech. Phys. Lett.* **15** 731 (1989); *Pis'ma Zh. Tekh. Fiz.* **15** (9) 64 (1989)
271. Ivanov B A, Kulagin N E *J. Exp. Theor. Phys.* **85** 516 (1997); *Zh. Eksp. Teor. Fiz.* **112** 953 (1997)
272. Zhukov A et al. *Nanoscale Res. Lett.* **7** 223 (2012)
273. Hubert A, Schäfer R *Magnetic Domains: the Analysis of Magnetic Microstructures* (Berlin: Springer, 2013)
274. Christian D A, Novoselov K S, Geim A K *Phys. Rev. B* **74** 064403 (2006)
275. Novoselov K S et al. *Nature* **426** 812 (2003)
276. Dillon J F, Remeika J P *J. Appl. Phys.* **34** 637 (1963)
277. Lisovskii F V, Mansvetova E G, Pak Ch M *J. Exp. Theor. Phys.* **81** 567 (1995); *Zh. Eksp. Teor. Fiz.* **108** 1031 (1995)
278. Logunov M et al. *Solid State Phenom.* **190** 737 (2012)
279. Gerasimov M V et al. *Instrum. Exp. Tech.* **60** 716 (2017); *Prib. Tekh. Eksp.* (5) 106 (2017)
280. Skyrme T H R *Nucl. Phys.* **31** 556 (1962)
281. Wiesendanger R *Nat. Rev. Mater.* **1** 16044 (2016)
282. Fischer J A et al. *Nat. Commun.* **7** 13000 (2016)
283. Sapozhnikov M V et al. *JETP Lett.* **107** 364 (2018); *Pis'ma Zh. Eksp. Teor. Fiz.* **107** 378 (2018)
284. Luo S et al. *Nano Lett.* **18** 1180 (2018)

285. Shen M et al. *Appl. Phys. Lett.* **112** 062403 (2018)
286. Zhang X et al. *Nanotechnology* **28** 08LT02 (2017)
287. Villard P et al. *IEEE J. Solid-State Circuits* **45** 214 (2010)
288. Chen T et al. *Proc. IEEE* **104** 1919 (2016)
289. Grollier J, Cros V, Fert A *Phys. Rev. B* **73** 060409 (2006)
290. Georges B et al. *Appl. Phys. Lett.* **92** 232504 (2008)
291. Lebrun R et al. *Nat. Commun.* **8** 15825 (2017)
292. Tsunegi S et al. *Sci. Rep.* **8** 13475 (2018)
293. Zahedinejad M et al., arXiv:1812.09630
294. Kaka S et al. *Nature* **437** 389 (2005)
295. Safin A R, Udalov N N, Kapranov M V *Eur. Phys. J. Appl. Phys.* **67** 20601 (2014)
296. Belanovsky A D et al. *Phys. Rev. B* **85** 100409 (2012)
297. Belanovsky A D et al. *Appl. Phys. Lett.* **103** 122405 (2013)
298. Abreu Araujo F et al. *Phys. Rev. B* **92** 045419 (2015)
299. Slavin A, Tiberkevich V *IEEE Trans. Magn.* **45** 1875 (2009)
300. Evelt M et al. *Sci. Rep.* **8** 1269 (2018)
301. Evelt M et al. *Phys. Rev. Appl.* **10** 041002 (2018)
302. Tulapurkar A A et al. *Nature* **438** 339 (2005)
303. Miwa S et al. *Nat. Mater.* **13** 50 (2013)
304. Jenkins A S et al. *Nat. Nanotechnol.* **11** 360 (2016)
305. Mitrofanov A A et al. *J. Appl. Phys.* **122** 123903 (2017)
306. Tamaru S et al. *Sci. Rep.* **5** 18134 (2015)
307. Louis S et al. *Appl. Phys. Lett.* **113** 112401 (2018)
308. Fang B et al. *Phys. Rev. Appl.* **11** 014022 (2019)
309. Choi H S et al. *Sci. Rep.* **4** 5486 (2014).
310. Locatelli N, Cros V, Grollier J *Nat. Mater.* **13** 11 (2013)
311. Zakeri K *Physica C* **549** 164 (2018)
312. Gomonay E V, Loktev V M *Low Temp. Phys.* **40** 17 (2014); *Fiz. Nizk. Temp.* **40** 22 (2014)
313. Costa C H O et al. *Solid State Commun.* **150** 2325 (2010)
314. Zakeri K *J. Phys. Condens. Matter* **29** 013001 (2016)
315. Zakeri K et al. *Phys. Rev. Lett.* **104** 137203 (2010)
316. Wu Y et al. *Adv. Mater.* **29** 1603031 (2016)
317. Walowski J, Münzenberg M *J. Appl. Phys.* **120** 140901 (2016)
318. Němec P et al. *Nat. Phys.* **14** 229 (2018)
319. Jungfleisch M B, Zhang W, Hoffmann A *Phys. Lett. A* **382** 865 (2018)
320. Zelezný J et al. *Nat. Phys.* **14** 220 (2018)
321. Turov E A et al. *Simmetriya i Fizicheskie Svoistva Antiferromagnetikov* (Symmetry and Physical Properties of Antiferromagnetic Materials) (Moscow: Fizmatlit, 2001)
322. Shamsutdinov M A et al. *Ferro- i Antiferromagnitodinamika. Nelineinye Kolebaniya, Volny i Solitony* (Ferro- and Antiferromagnetodynamics. Nonlinear Oscillations, Waves, and Solitons) (Moscow: Nauka, 2009)
323. Kosevich A M et al. *Nelineinye Volny Namagnichennosti. Dinamicheskie i Topologicheskie Solitony* (Nonlinear Magnetization Waves. Dynamic and Topological Solitons) (Kiev: Naukova Dumka, 1983)
324. Khymyn R et al. *Sci. Rep.* **7** 43705 (2017)
325. Khymyn R, Tiberkevich V, Slavin A *AIP Adv.* **7** 055931 (2017)
326. Khymyn R et al. *Phys. Rev. B* **93** 224421 (2016)
327. Lebrun R et al. *Nature* **561** 222 (2018)
328. Patil R A et al. *Nanoscale* **8** 12970 (2016)
329. Sulymenko O R et al. *Phys. Rev. Appl.* **8** 064007 (2017)
330. Beaurepaire E et al. *Appl. Phys. Lett.* **84** 3465 (2004)
331. Stremoukhov P A et al. *J. Appl. Phys.* **125** 223903 (2019)
332. Ross A et al. *Nano Lett.* **20** 306 (2020)
333. Chen Z, Harris V G *J. Appl. Phys.* **112** 081101 (2012)
334. Lutsev L V et al. *J. Magn. Magn. Mater.* **300** e12 (2006)
335. Sakharov V K et al. *IEEE Magn. Lett.* **8** 3704105 (2017)
336. Kumar N et al. *J. Magn. Magn. Mater.* **272** E899 (2004)
337. Dobrovolskiy O V et al. *Sci. Rep.* **7** 13740 (2017)
338. Dobrovolskiy O V et al. *Nat. Phys.* **15** 477 (2019)
339. Zholud A et al. *Phys. Rev. Lett.* **119** 257201 (2017)
340. Bender S A, Duine R A, Tserkovnyak Y *Phys. Rev. B* **99** 024434 (2019)
341. Qaiumzadeh A, Brataas A *Phys. Rev. B* **98** 220408 (2018)
342. Mondal P et al. *Phys. Rev. B* **99** 094431 (2019)
343. Garcia-Sanchez F et al. *Phys. Rev. Lett.* **114** 247206 (2015)
344. Han W et al. *Nat. Nanotechnol.* **9** 794 (2014)
345. Evelt M et al. *Phys. Rev. B* **95** 024408 (2017)
346. Zhou B et al. *J. Phys. Condens. Matter* **22** 445302 (2010)
347. Tombros N et al. *Nature* **448** 571 (2007)
348. Morozov S V *Phys. Usp.* **55** 408 (2012); *Usp. Fiz. Nauk* **182** 437 (2012)